

Mechanisms of evolution of the propeller wake in the transition and far fields

M. FELLI^{†1}, R. CAMUSSI² AND F. DI FELICE¹

¹CNR-INSEAN, Italian Ship Model Basin, Via di Vallerano 139, 00128 Rome, Italy

²Dipartimento di Ingegneria Meccanica e Industriale, Università Roma Tre,
Via della Vasca Navale 79, 00146, Italy

(Received 4 December 2009; revised 4 March 2011; accepted 22 March 2011)

In the present study the mechanisms of evolution of propeller tip and hub vortices in the transitional region and the far field are investigated experimentally. The experiments involved detailed time-resolved visualizations and velocimetry measurements and were aimed at examining the effect of the spiral-to-spiral distance on the mechanisms of wake evolution and instability transition. In this regard, three propellers having the same blade geometry but different number of blades were considered. The study outlined dependence of the wake instability on the spiral-to-spiral distance and, in particular, a streamwise displacement of the transition region at the increasing inter-spiral distance. Furthermore, a multi-step grouping mechanism among tip vortices was highlighted and discussed. It is shown that such a phenomenon is driven by the mutual inductance between adjacent spirals whose characteristics change by changing the number of blades.

Key words: vortex breakdown, vortex dynamics, vortex instability

1. Introduction

The knowledge of the mechanisms of wake instability behind rotor systems, such as propellers, wind turbines or helicopters rotors, plays an important role in many engineering applications because of its direct correlation to performance, vibrations, noise and structural problems.

From the physical point of view, the wake generated by a single rotor blade consists of two systems of vortical structures at the root and tip sections and a sheet of trailing vortices shed spanwise as the consequence of the non-constant circulation that usually characterizes the operating range of a rotor. This vortex system forms a helical vortex sheet surface that undergoes a complex process of roll-up, dividing the flow into a strong central vortex and distinct embedded tip vortices (see e.g. Kerwin 1986; Conlisk 1997; Vermeer, Sorensen & Crespo 2003).

The study of the rotor wake evolution has received some attention in the literature and a number of empirical and theoretical analyses dealing with the problem of the development and the dynamics of the wake structures in the near field have been reported (Landgrebe 1972; Kobayashi 1982; Jessup 1989; Chesnakas & Jessup 1998; Leishman 1998; Stella *et al.* 2000; Di Felice *et al.* 2004; Felli *et al.* 2006).

Recent advances in the stability analysis of helical tip vortices pointed out that the stability of a rotor wake is the consequence of the mutual interaction among

[†] Email address for correspondence: m.felli@insean.it

the tip and hub vortices and the helical filaments trailing from each blade (Lugt 1996; Okulov & Sørensen 2007). This mutual interaction stabilizes the system of multiple helical tip vortices in a rotor wake, otherwise unstable independent of the filament number, the core diameter, the disturbance type and the occurrence of the hub vortex, as widely proved in the literature (Levy & Forsdyke 1928; Widnall 1972; Gupta & Loewy 1974; Okulov 2004; Okulov & Sørensen 2007). In this regard, considering a model with N helical tip vortices embedded in a helical vortex field formed by the trailing vortex sheet of the blades and the root vortices, Okulov & Sørensen (2007) demonstrated the existence of stable tip vortices. Therefore, the unconditionally unstable model of Joukowski (1912) was based on the assumption that the circulation is constant over the blade span and that the wake only consists of a root and a tip vortex stabilizes if the contribution of the trailing vortex sheet is considered. It is worth noting that even though the flow configurations might be significantly different, most of the stability models and theories concerning the stability of helical vortices can be applied not only to propellers but also to helicopter rotors and wind turbines (see Okulov 2004; Okulov & Sørensen 2007, 2010 for wind turbine rotors; and Leishman *et al.* 1998 for helicopter rotors).

In spite of a number of studies dealing with the problem of the instability of helical vortex systems, the identification of the triggering mechanism of the rotor wake instability as well as the reconstruction of the complex dynamics of the propeller structures in the transition and the far wake are still open problems in the fluid dynamics research, not yet explained or described thoroughly in the literature. Indeed, the adoption of simplified theoretical models is not adequate to represent the wake evolution in the transition region and the far field, where the progressive distortion of the wake from the helical geometry with radial and longitudinal variations of the pitch, the auto and mutual interaction effects among the vortical structures, the complex deformation of the tip and hub vortices, the effect of turbulence and viscosity have to be considered for a correct description of the problem. Owing to the complexity of the flow field, the support of complex theoretical models and very advanced experimental techniques are required for a thorough understanding of the problem of the rotor wake instability and far-field evolution mechanisms.

The analysis of the state of the art reveals some open problems and a number of basic questions arise from the lack of understanding of this specific problem. Specifically these are as follows.

(i) *Rotor wake transition to instability.* The mechanisms leading to the instability of a rotor wake have not been described yet in the literature. Recent experimental works provide a description of some typical features of the propeller wake in the transition and far fields, as the occurrence of a precession motion of the propeller streamtube around the hub vortex spiral coupled with the energy transfer from the blade to the shaft harmonic (Felli *et al.* 2006). However, no explanation on the nature of the perturbation triggering to the wake instability and its mechanism of propagation has been given yet. Di Felice *et al.* (2004) hypothesized a strict correlation between the transition to instability and the interaction between the trailing wake of the actual blade and the tip vortex of the previous one which occurs as the consequence of the different pitch angle of their helical paths. Pressure measurements (Felli *et al.* 2006) and flow visualizations (Stella *et al.* 2000) support this thesis, which revealing dependence of some typical features of the wake instability (e.g. phase shift of the tip vortex, blade-to-shaft harmonic energy transfer, destabilization of the hub vortex, precession of the streamtube) on the aforementioned mechanism of mutual interaction between the tip vortex and the trailing wake of the successive blade. Therefore, the

distance between two consecutive blade wakes seems to play a role in the slipstream instability mechanism, especially at the starting point of the tip and hub vortex destabilization.

(ii) *Wake evolution in the transition and the far regions.* The dynamics of the propeller vortices is a complex phenomenon in which the effect of the viscosity, the mechanisms of auto and mutual induction (Widnall 1972), the effect of torsion (Ricca 1994) have to be accounted for and described during the evolution down to the breakdown. This is a difficult task for both a theoretical and an experimental approach, justifying the lack of studies dealing with this aspect in the literature, especially for what concerns the transition and the far wakes. Indeed, the state of the art on the problem of the rotor wake evolution is limited to the near wake and to the development of simplified models. On the theoretical side, the state of the art has progressed from the early momentum and vortex theories (Rankine 1865; Froude 1889; Glauert 1927; Goldstein 1929; Mangler & Squire 1953; Pizali & Duwaldt 1962; Miller, Tang & Perlmutter 1968) to advanced models with a distorted geometry of the wake, in which each blade releases a sheet of vortex filaments free to interact and distort until converging to a deformed geometry. These models include the tip vortex roll-up and the distortion of the wake shed from the inboard sections (Landgrebe 1972; Kerwin 1986). On the experimental side, the support of advanced optical techniques and flow visualizations allowed a quite detailed reconstruction of the rotor structure dynamics in the near wake of marine propellers, helicopter rotors and wind turbines. The mechanism of the tip vortex rolls up was investigated by Kobayashi (1982), Cenedese, Accardo & Milone (1985), Jessup (1989), Chesnakas & Jessup (1998), Stella *et al.* (2000). In these papers, the problem of wake evolution was analysed through velocity measurements along transversal planes in the near wake of a marine propeller. Di Felice *et al.* (2004) studied the propeller wake evolution along a diametral plane of the wake for different swirl numbers. Felli *et al.* (2006) re-proposed the experiment of Di Felice *et al.* (2004) investigating the phase correlations between velocity and pressure signals. Vermer *et al.* (2003) tackled the problem of the aerodynamics of a wind turbine. The problem of the rotor wake instability was tackled experimentally by Ortega (2001) for a two-bladed propeller and re-proposed by Felli *et al.* (2008) that analysed the power spectra of the velocity signals streamwise down to the far wake.

(iii) *Tip and hub vortex breakdown.* The basic underlying mechanism leading to tip and hub vortex breakdown in a rotor wake is still not known completely. Flow visualizations have provided some global information on the location where the hub vortex breaks down (Stella *et al.* 2000). However, the behaviour of the tip vortices as well as the physical mechanism or mechanisms leading to the propeller wake breakdown is still unknown. This is mainly due to the fact that measurements, whether invasive (e.g. hot wires) or non-invasive (e.g. LDV), and flow visualizations are difficult to obtain and interpret in such a complex, unsteady, three-dimensional (3D) flow.

In this paper, we experimentally investigate the above aspects through velocity measurements and high-speed visualizations. The study was performed on a reference model of a marine propeller, widely studied in the literature with the most advanced experimental (Cenedese *et al.* 1985; Stella *et al.* 2000; Di Felice *et al.* 2004; Pereira, Salvatore & Di Felice 2004a; Pereira *et al.* 2004b) and numerical techniques (Salvatore *et al.* 2003, 2006; Greco *et al.* 2004; Bensow, Liefvendahl & Wikstrom 2006).

In order to analyse the instability mechanisms at different inter-spiral distances, the number of blades was varied from two to four.

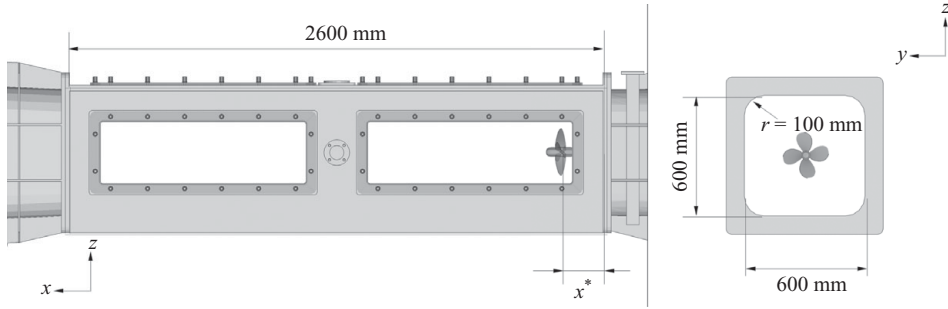


FIGURE 1. Test section facility.

The laboratory study conducted in controlled flow conditions has a practical relevance, since in real situations the position at which the tip vortex system destabilize depends, besides the loading conditions, largely on the propeller geometry and the blade number. The destabilization of the tip vortex system can occur even very close to the trailing edge of the propeller blades and, thus, it may influence the performance of the rudder and the hull. For instance, this is the case of highly skewed propellers or propeller/rotors having a large number of blades. Furthermore, the grouping mechanism induced by the destabilization may influence the acoustic signature of a propeller in submarines (Liefvendahl, Felli & Troëng 2010). In addition, for installed propellers, the perturbation of the incoming flow may influence the position at which the wake destabilizes. However, the analysis of instability mechanisms in more realistic configurations is quite complex and remains a challenge for future studies.

This work is organized as follows. In § 2, we deal with the description of the propeller model, the measurement techniques and the experimental set-up. The problem of the propeller wake instability and breakdown is addressed in §§ 3 and 4. The problem was tackled through the analysis of high-speed visualizations in the transition and the far wake and phase-averaged velocity measurements, at different blade numbers. In addition, a thorough data analysis was performed on velocity time histories.

Different indicators such as power spectral density (PSD), phase trajectories (PT), Lyapunov exponents (LE) (Bergé, Pomeau & Vidal 1984; Hilborn 2000) were adopted. A description of such mathematical tools is provided in § 3. Conclusions and final remarks are presented in § 5.

2. Experimental set-up and test conditions

2.1. Facility

The tunnel, a Kempf & Remmers close jet-type circuit, having dimension $12 \text{ m} \times 8 \text{ m}$, is developed along a vertical plan. The test section is 2.6 m long and has a square cross-section of $0.6 \times 0.6 \text{ m}^2$ (figure 1). Eight Perspex windows on the four walls (two for each side) enable the optical access. The nozzle contraction ratio is $5.96 : 1$ and the maximum water speed is 12 m s^{-1} . The highest free-stream turbulence intensity in the test section is less than 2%. In the test section, the mean velocity uniformity is within 1% for the axial component and 3% for the vertical component.

In the present experimental set-ups, the propeller was installed on a J15 model Kempf & Remmers dynamometer, having 2450 N maximum thrust, 98 N m maximum torque and 4000 r.p.m. maximum speed, at $x = 200 \text{ mm}$ downstream of the test section entrance.

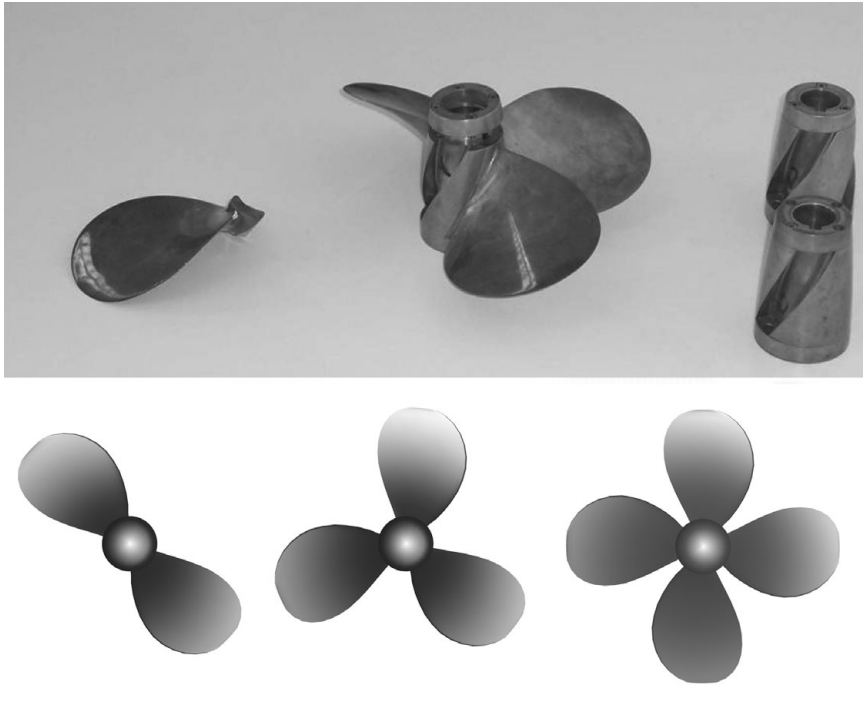


FIGURE 2. Blade configurations of the E779 propeller.

2.2. Propeller model

The propeller used for the experimental activity was derived from the E779a model. This is a Wageningen modified type, four bladed, fixed-pitch, right-handed propeller, characterized by a nominally constant pitch distribution and a very low skew. This model propeller was chosen for two main reasons. First, this propeller was widely studied in the past using advanced experimental techniques and has been referred to in a number of papers in the literature (Cenedese *et al.* 1985; Stella *et al.* 2000; Di Felice *et al.* 2004; Pereira *et al.* 2004a,b; Felli *et al.* 2006). Second, this model propeller, highly loaded at the tip, sheds strong tip vortices and, hence, it is particularly suitable for the study of the wake instability and breakdown phenomena, where the dynamics of the tip vortices is considered to play an important role. The propeller was assembled into different configurations, with different number of blades. This solution was developed by designing three special hubs whose geometries allow arrangement of the blades in configurations with two, three and four elements, respectively. A picture of the three propeller configurations is given in figure 2.

The geometrical characteristics of the propellers are given in table 1; further information (i.e. radial distribution of chords, pitch, skew, blade section camber and thickness forms) is documented in Salvatore *et al.* (2006).

The performance characteristics were determined for the three configurations of the E779a propeller. The different values of the advance coefficient were obtained varying the facility speed and keeping the propeller rotational speed constant at $n = 25$.

The propeller coefficients (i.e. thrust (Kt), torque (Kq) and efficiency ([η])) versus the advance ratio are illustrated in figure 3(a). Obviously, the intensity of the propeller thrust coefficient increases with the increasing blade number. However, the dependence

Propeller diameter	$D = 227.27$ mm
Number of blades	$Z = 2, 3, 4$
Rake (nominal)	$i = 4^\circ 35'0''$ (forward)
Expanded area ratio	$EAR = 0.689$
Hub diameter (at prop. ref. line)	$D_H = 45.53$ mm
Pitch ratio (nominal)	$P/D = 1.1$

TABLE 1. Dimensions of the INSEAN E779a model propeller.

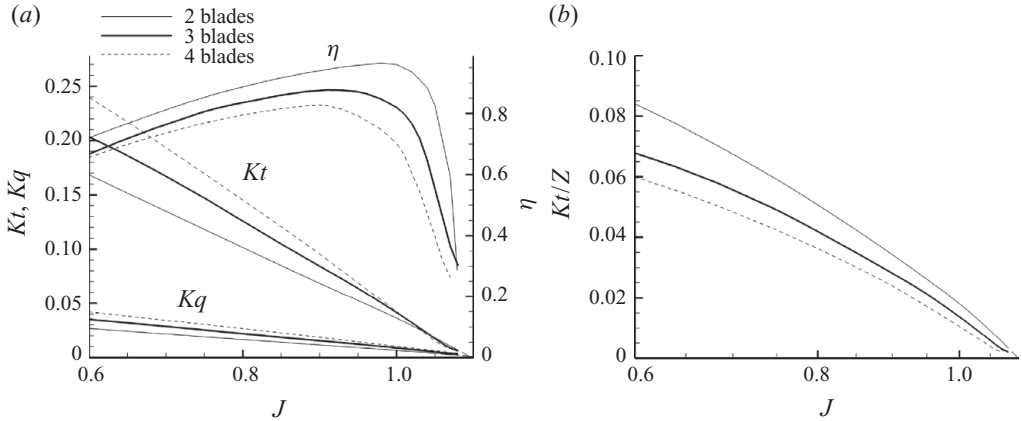


FIGURE 3. (a) Performance characteristics and (b) thrust coefficient per blade for the two-, three- and four-bladed propellers.

of the propeller thrust on the blade number is not linear due to the blade-to-blade interaction that induces performance decay as the blade number increases. This behaviour is illustrated in figure 3(b), which represents the thrust coefficient per blade versus the advance ratio. In this case, increasing the blade number results in a decay of the thrust.

This trend is particularly apparent at low J (highly loaded propellers) where a larger deviation among the diagrams of the three propellers is observed. The reduced hydrodynamic pitch of the propeller wake at low J and, consequently, the stronger inter-blade induction effects explain this behaviour.

Additional tests were performed in order to quantify the effect of the Reynolds number on measured loads. In particular, measurements were repeated for three different values of the propeller rotational speed, corresponding to 12, 25 and 30 revolutions per second (r.p.s.). Measured thrust coefficients are compared in figure 4.

The analysis shows that the effect of Reynolds number becomes definitively negligible above a ‘critical’ value. Actually, the deviation among the diagrams of the thrust coefficient versus the advance ratio, nearly zero for $n = 25$ and 30, increases sensibly when the rotating velocity of $n = 12$ is considered. This behaviour is due to the laminar portion of the boundary layer at the blade’s leading edge, as observed by Di Felice *et al.* (2004). In fact, its extension depends on the local Reynolds number and, in particular, it reduces as the Reynolds number increases. The variability of the propeller thrust and torque as to the Reynolds number, widely discussed in the literature, is typically experienced during open-water tests in towing tanks on medium-size propeller models. Comments on this subject may be found e.g. in the Report of the Propulsion Committee of the 23rd ITTC (2002).

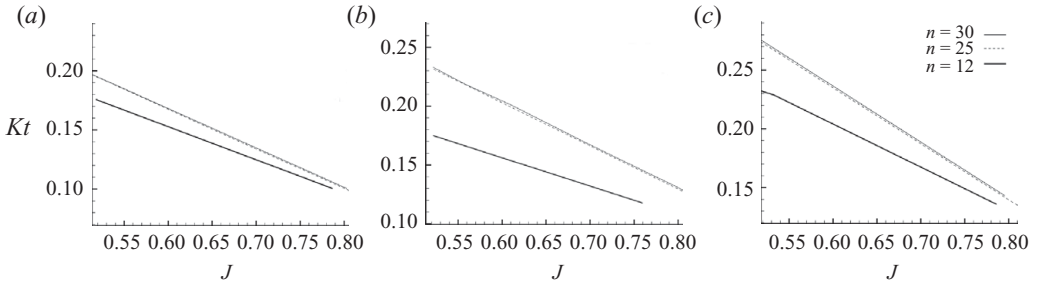


FIGURE 4. Effect of the Reynolds number on the thrust coefficient: two- (a), three- (b) and four- (c) bladed propellers.

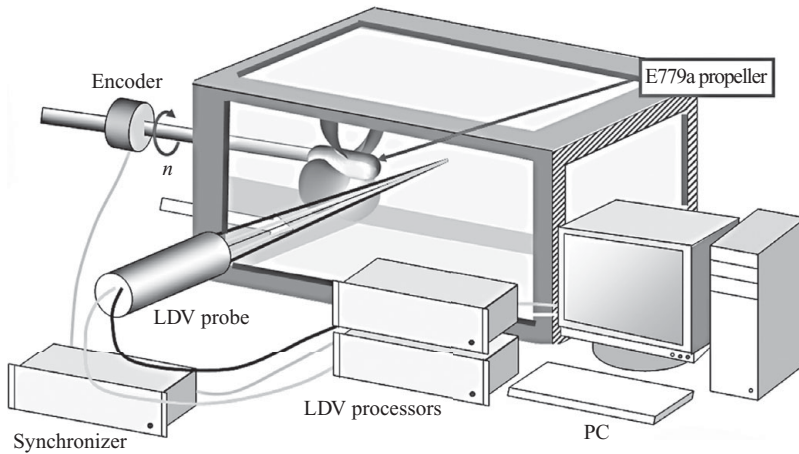


FIGURE 5. Experimental set-up for the LDV measurements.

2.3. Velocity measurements

Flow velocities were measured by means of a two-component back-scatter laser Doppler velocimeter (LDV, which consists of a 6 W argon laser, a fibre optic probe, a 40 MHz Bragg cell for the velocity versus ambiguity removal and a digital burst correlator signal processor). The experimental set-up of the LDV tests is sketched in figure 5.

The probe works in a back-scatter mode and allows measurement of two orthogonal velocity components simultaneously. Specifically, it was arranged to measure the axial and vertical components of the velocity in a fixed frame. In view of the axisymmetrical propeller inflow, the reconstruction for the 3D field in a transversal plane behind the propeller can be carried out sweeping the measurement volume along two orthogonal radial directions: along a vertical radius for the axial and radial components and along a horizontal radius for the axial and tangential components (Cenedese *et al.* 1985). Therefore, all measurements at a certain radius can be conducted without moving the LDV volume, acquiring the angular position of the reference blade and using phase sampling techniques (PST). This was carried out by a rotary 7200 pulse/revolution encoder and a synchronizer that provides the digital signal of the propeller position to the TSI RMR (rotating machine resolver).

The correspondence between the randomly acquired velocity bursts and the propeller angular position was carried out by using the TTT (tracking triggering

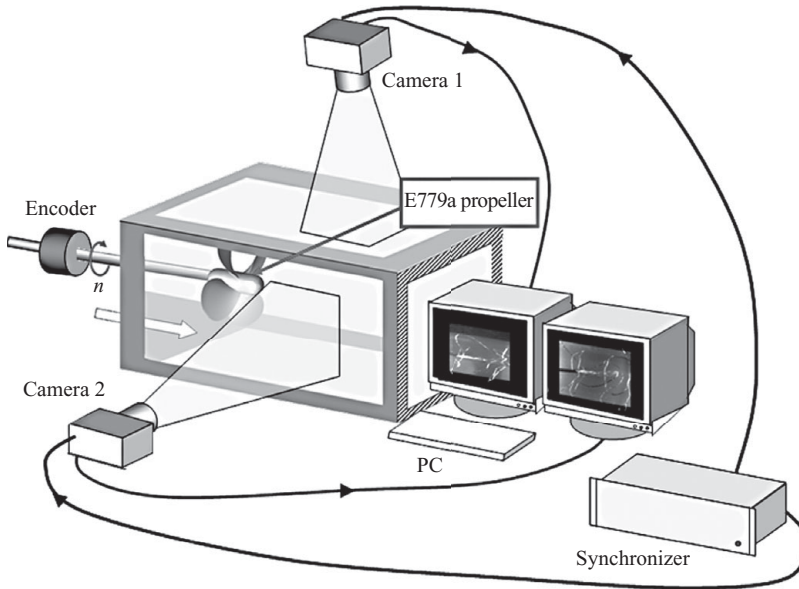


FIGURE 6. Experimental set up for the high-speed visualizations.

technique) phase sampling technique (Stella *et al.* 2000; Felli & Di Felice 2005). Details about this technique are provided in §3.4. The LDV probe was set up on a computer-controlled traversing system which allows obtaining a displacement accuracy of 0.01 mm in the three axes and to achieve a high automation of the LDV system. The seeding particles size and concentration were controlled in the facility: the water was filtered before the measurements (3 μm low-pass) and seeded with 10 μm silver hollow coated glass particles. Water seeding was performed at the start of the tests, because it was observed that the density of the seeding particles remains almost constant for a long time in the facility. Data acquisition was accomplished by using a personal computer, while the post-processing analysis, requiring several gigabytes of data storage and computational resources, was performed on a workstation.

2.4. High-speed visualizations

Flow visualizations were undertaken making the tip vortices cavitating by varying the pressurization of the facility. Figure 6 shows a sketch of the camera arrangement in the test section. Visualizations were performed by means of two high-speed CMOS cameras, arranged to image the test section from two orthogonal directions. The cameras were two Photron-Ultima APX having a maximum resolution of $1024 \times 1024 \text{ pixel}^2$ up to $2000 \text{ frames s}^{-1}$. Cameras were equipped with a 60 mm lens with 2.8 f-number. The synchronization between the two devices was accomplished by an external impulse that triggers the acquisition of the first (master) and second camera (slave), at the desired frame rate and with a selected delay (in the present case $\Delta t = 0$). Three 1000 W lamps were used to light the investigated area with the aim to ensure a homogeneous distribution of the light over the imaged area and an adequate quality of the visualizations up to a frame rate of 4000 Hz. During the visualizations, the static pressure of the facility was modulated depending on the propeller blade configuration and ranged between 0.4 and 0.7 bar. This ensured an adequate identification of the propeller vortical structures during their evolution, without compromising the quality of the images for the occurrence of air bubbles.

2.5. Reference frames and dimensionless groups

Two reference systems were adopted.

(i) A Cartesian reference frame $O-XYZ$ with the origin O at the intersection between the propeller disk and the rotation axis, the X axis downstream-oriented along the tunnel centreline, the Y axis along the upward vertical and the Z axis along the horizontal towards starboard.

(ii) A cylindrical reference frame $O-XR\theta$ with the origin O in the intersection between the propeller disk and the rotation axis, the X axis downstream-oriented along the propeller axis, the R axis along the radial outward and the θ axis along the azimuth.

Two dimensionless groups govern the rotor flow field in non-cavitating conditions: the advance ratio $J = U_\infty/2nR$, where U_∞ is the free-stream velocity, n is the revolution frequency and $2R$ is the rotor diameter and the Reynolds number $Re = C_{0.7}V_{0.7}/\nu$, where $C_{0.7}$ and $V_{0.7}$ are the chord of the blade and the velocity at $0.7 r/R$, respectively, and ν is the kinematic viscosity.

3. Mathematical tools for the dynamical analysis of the propeller wake evolution

The mechanism of the propeller wake instability is characterized through the application of the following mathematical tools commonly adopted for the analysis and the classification of dynamical systems: PSD, PT, LE and PST. A short description of the procedures is given in the following paragraphs, leaving the details to the wide bibliography available in the field.

3.1. Power spectral density

The Fourier PSD was performed on the time histories of the velocity signals. The random sampling times in LDV preclude the use of standard spectral methods for even-spaced samples and require the implementation of spectral estimators for randomly sampled data. In this regard, the power spectrum of the randomly acquired LDV signals was estimated using the ‘slotted time’ method as in Gastor & Roberts (1977). In this algorithm, data pairs are grouped according to the time window into which their time difference falls. The width of the time window equals the time delay increment of the digital autocorrelation, so that the correlation estimate is smoothed over this time and the PSD, computed by Fourier transforming the estimated correlation, is a windowed estimate. The random nature of the LDV signal allowed removal of the Nyquist sampling requirement and obtaining a good estimation of the power spectrum in the range of frequencies of interest. Also, long records (i.e. about 10 min) were necessary to achieve an acceptable statistical convergence.

3.2. Phase trajectories

The phase space is a mathematical space in which each orthogonal coordinate represents a degree of freedom of a dynamical system. Usually, the number of degrees of freedom is not known *a priori* and it is necessary to reconstruct both the phase space and the topology of the attractor by using a time delay technique (Takens 1981; Bergé *et al.* 1984) from the values of the variable $x(t)$ at the instant t and at $n - 1$ uncorrelated instants. Then, a phase pseudo-space (i.e. the phase space reconstructed by the time delay technique) is defined as

$$X(t) = \{x(t), x(t + \tau), \dots, x(t + (n - 1)\tau)\}. \quad (3.1)$$

The time delay τ is typically given by the first zero of the autocorrelation function, calculated for each signal systematically (Bergé *et al.* 1984). In this case, the behaviour of the dynamic system is described in a 3D projection of the pseudo-phase space through the evolution of the phase trajectories.

A first-order polynomial interpolation of the velocity signals was used in order to reconstruct a continuous time series to resample at even-time intervals.

3.3. Lyapunov exponents (LE)

For a dynamical system, sensitivity to initial conditions is quantified by the Lyapunov exponents. When the attractor is chaotic, two trajectories with nearby initial conditions tend to diverge, on average, at an exponential rate characterized by the largest Lyapunov exponent (Bergé *et al.* 1984). This concept is also generalized for the spectrum of Lyapunov exponents, λ_i ($i = 1, 2, \dots, n$), by considering a small n -dimensional sphere of initial conditions, where n is the number of state variables used to describe the system. As time (t) progresses, the sphere evolves into an ellipsoid whose principal axes expand (or contract) at rates given by the Lyapunov exponents. The presence of a positive exponent is sufficient for diagnosing chaos and represents local instability in a particular direction.

In the present case, the adopted procedure to evaluate the sensitivity to the initial conditions is to estimate the maximal Lyapunov exponent according to the method proposed by Rosenstein, Collins & De Luca (1993). This consists in estimating directly the separation between pairs of neighbouring points in state space as they diverge over time. By plotting the log of the divergence versus time the maximal Lyapunov exponent is estimated by computing a least-squares fit to the linear region of the resulting curve.

3.4. Phase sampling techniques

The TTT was implemented to phase the randomly acquired velocity bursts with the angular position of the reference blade. Velocity samples were acquired when Doppler signal was detected in any of the two LDV channels and tagged with the angular position of the reference blade at the measurement time. Once acquired, velocity data were arranged inside angular slots of constant width and here statistically processed by ensemble averaging. The average was achieved by a large number of repeated experiments (i.e. 15000 statistical events considering an acquisition time of 600 s and a propeller revolution speed of 25 r.p.s.), where each one is a complete revolution of the propeller. An exhaustive description of the TTT technique and the slotting procedures can be found in Stella *et al.* (2000) and Felli & Di Felice (2005). In the present analysis, statistical processing was performed using 360 overlapped slots of $2\varepsilon = 2^\circ$ width and implementing a weighted average with Gaussian law to determine the influence of each velocity sample with the distance from the slot centroid.

This choice was proved adequate to describe accurately flow regions with high gradient. The statistical population ranged from 1000 to 1500 samples per slot, depending on the local frame rate of the LDV system.

4. Analysis of the propeller wake instability and breakdown mechanisms

The problem of the propeller wake instability and breakdown is addressed in the following paragraphs through the analysis of time-resolved visualizations (§4.1) and time histories of velocity signals (§4.2).

4.1. Analysis of the time-resolved visualizations

Time-resolved visualizations are a powerful tool for the detailed qualitative analysis of the tip and hub vortex dynamics in the transition and the far wake, providing accurate information on the mechanisms of the propeller wake instability and breakdown. In addition, this kind of information is particularly helpful to integrate, understand and interpret the results of the dynamical analysis that is presented in §4.2. The study aims at getting an insight into the main features of the tip and hub vortex destabilizing mechanisms as well as at highlighting any differences in the tip vortex evolution for different blade number configurations.

High-speed visualization involved an extensive collection of camera recordings at high frame rates (i.e. 2 kHz), and were acquired for a wide combination of loading conditions (i.e. $J = 0.45$, $J = 0.55$, $J = 0.65$, $J = 0.75$, $J = 0.85$), imaged areas and blade number configurations (i.e. $Z = 2$, $Z = 3$, $Z = 4$). In the following, for the sake of conciseness, only part of this extensive dataset, representative of the main features of the tip and hub vortex evolution, is shown.

4.1.1. Visualizations of the propeller wake instability modes

An overview of the wake evolution is shown in figures 7 and 8. The effect of the number of blades is shown in figure 7, where the evolution of the cavitating traces of the tip vortices is shown for $Z = 2$, $Z = 3$ and $Z = 4$. At a given Z , snapshots are referred to different instants, spaced every $\Delta t = 0.1T$ (where T is the revolution period).

In this case, the advance ratio of the three propellers (i.e. $J = 0.45$) was chosen to confine the wake evolution, from the trailing edge to the far wake, within a single window of the test section. Figure 8 shows the effect of the advance ratio for $Z = 2$, $Z = 3$ and $Z = 4$.

According to Okulov (2004), the transition to the instability shows clear dependence on the spiral-to-spiral distance. More specifically, the transition region moves downstream more and more when the spiral-to-spiral distance reduces. It follows that the blade number Z conditions the position of the onset of the wake instability. In fact, the blade number influences the spiral-to-spiral distance and the blade loading conditions (see figure 3*b*). The latter has an effect on the hydrodynamic pitch of the wake and, thus, on the spiral-to-spiral distance indirectly.

In the transition wake, the incoming instability of the propeller wake is featured by an abrupt destabilization of the vortex system. This is clearly shown in the visualizations of figures 7 and 8. In particular, (i) the tip vortices deform from the helical path and tend to interact mutually and form group; (ii) the hub vortex undergoes a sudden deformation from straight to a spiralling geometry.

On the basis of the available dataset of flow visualizations, a comparative estimation of the positions where the tip and hub vortex instability transitions occur was carried out for different blade number configurations. In this regard, the location of the instability inception point would be estimated referring to a typical feature of the instability process once an identification criterion is defined. In the present case, the following criteria were adopted to localize the instability inception point of the tip and hub vortices.

(i) *Tip vortices*. In the image plane, the envelope of tip vortices describes a curve $I_{tip}(x)$ (x is the axial coordinate in the image plane) whose slope is zero after the wake contraction and diverges suddenly where the tip vortex instability transition occurs (figure 9). The position x^* , at which the tip vortex destabilizes, was defined by identifying the first position at which such a divergence equals 50 % of the maximum

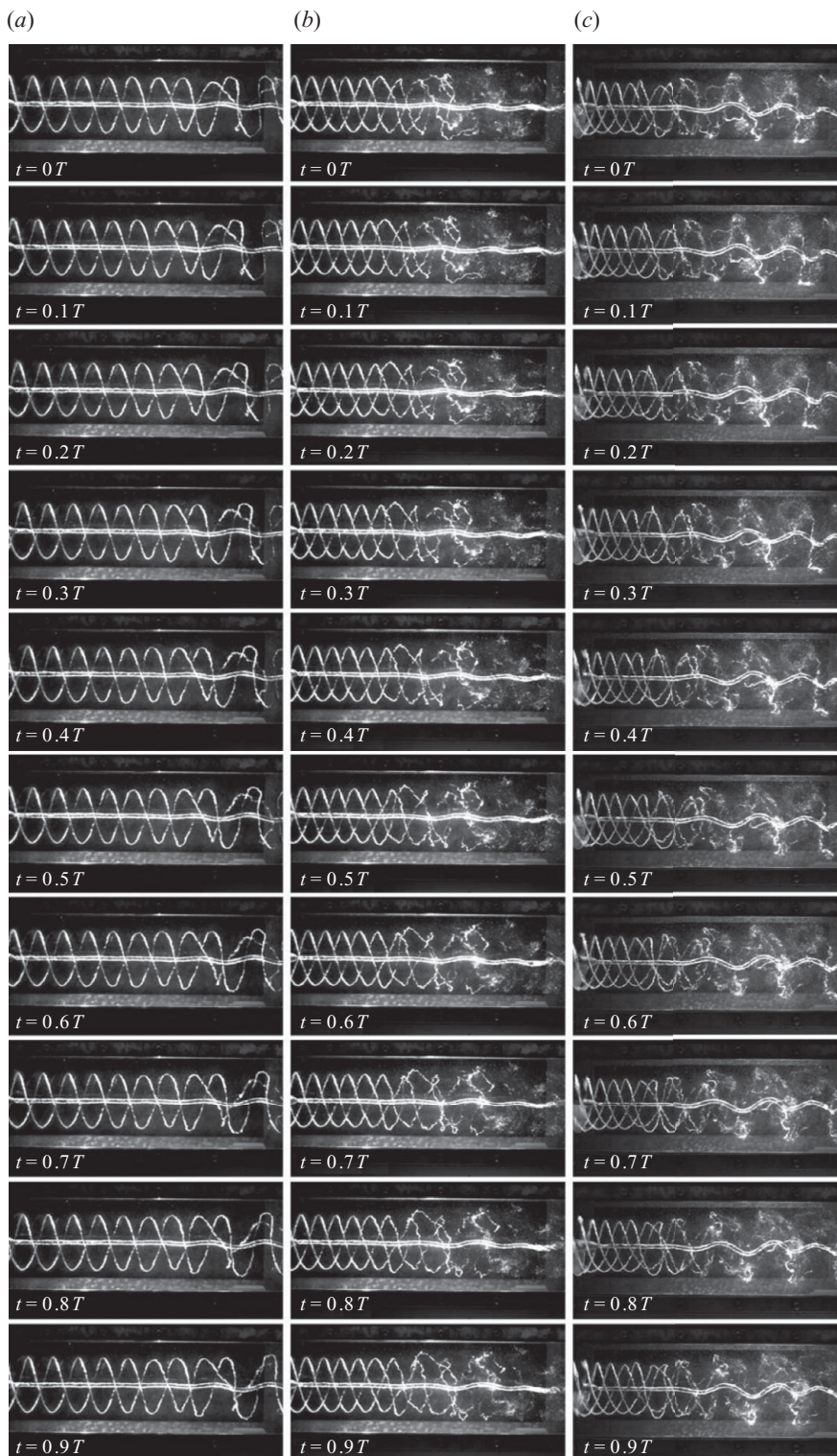


FIGURE 7. Propeller wake evolution of the two- (a), three- (b) and four- (c) bladed propellers at $J = 0.45$. The separation time delay between successive snapshots is $\Delta t = 0.1T$.

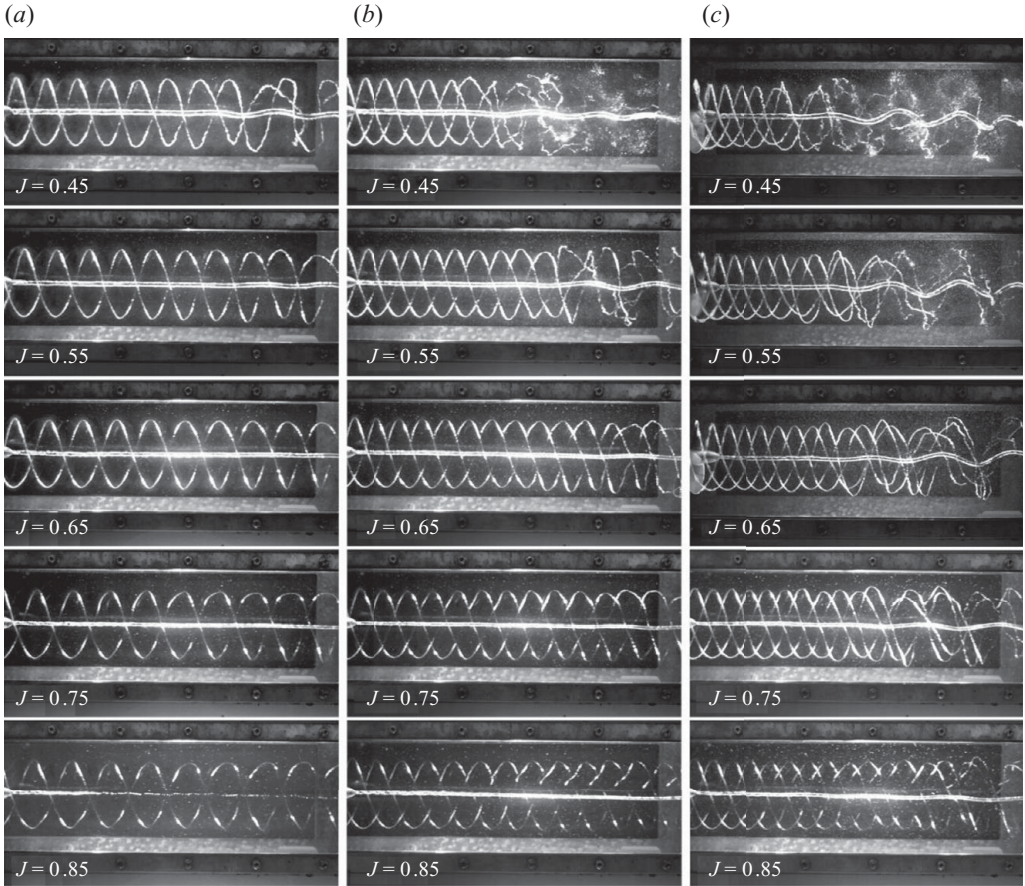


FIGURE 8. Effect of the advance ratio: single snapshot of the time-resolved wake evolution for $Z = 2$ (a), $Z = 3$ (b) and $Z = 4$ (c) at different values of J (i.e. $J = 0.45, 0.55, 0.65, 0.75$ and 0.85 , from top to bottom). The acquisition time of each snapshot as referred to in the propeller rotation period is generic.

slope of the tip vortex envelope:

$$\text{atan} \left(\frac{\partial I_{tip}(x^*)}{\partial x} \right) = 0.5 I_{tip}^{max}, \quad (4.1)$$

where I_{tip}^{max} is the maximum slope of tip vortex envelope. The curve $I_{tip}(x)$ was drawn from the standard deviation image calculated over 1000 snapshots in the time history of the visualizations of the wake evolution.

(ii) *Hub vortex*. The transition to instability of the hub vortex was defined according to the position at which it starts to deviate from the straight geometry. In the image plane, the boundary of the hub vortex trace describes a curve $I_{hub}(x)$ whose slope is zero in the near wake, where the vortex is straight, and starts to diverge suddenly from the transition point because of the hub vortex oscillations after the instability (Felli *et al.* 2006) (figure 9). Analogous to the case of the tip vortices, the position x^* of the hub vortex instability inception was defined according to the following criterion:

$$\text{atan} \left(\frac{\partial I_{hub}(x^*)}{\partial x} \right) = 0.5 I_{hub}^{max}, \quad (4.2)$$

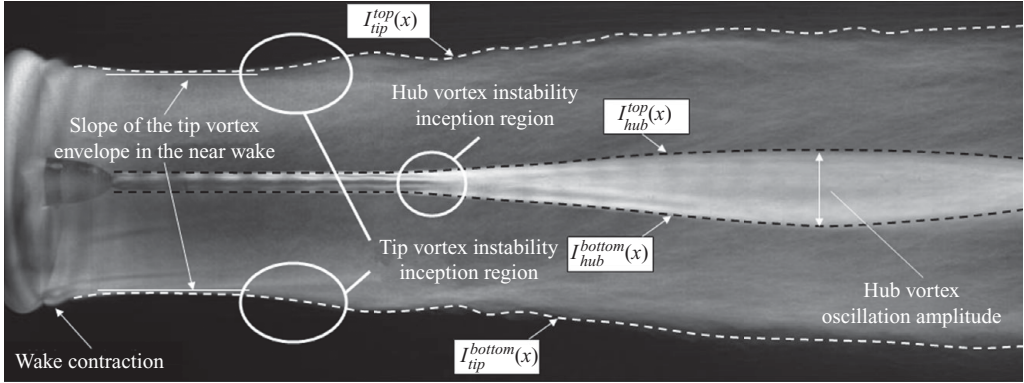


FIGURE 9. Identification criteria for the tip and hub vortex instability transition.

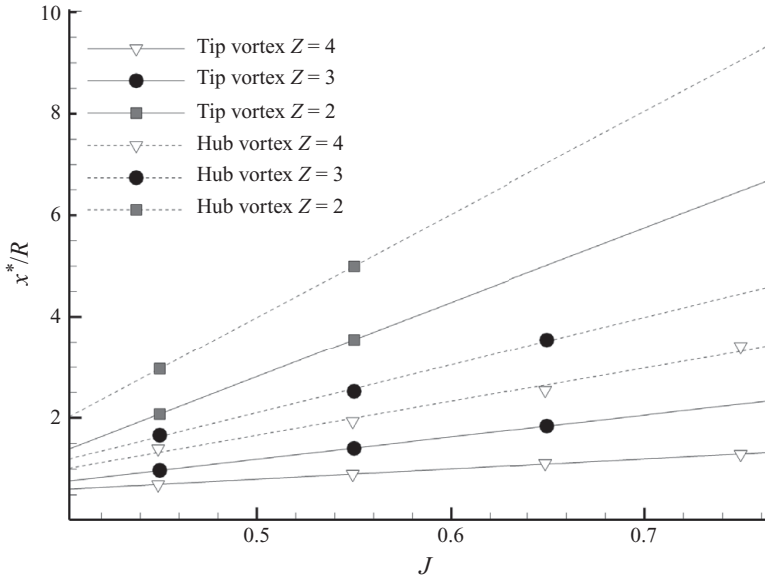


FIGURE 10. Dependence of the instability transition point x^*/R of the tip and hub vortices on the advance coefficient J . The location of the instability inception was estimated through a statistical approach, considering the positions where the tip and hub vortices start to deviate from the helical and straight geometries, respectively.

where I_{hub}^{max} is the maximum slope of tip vortex envelope. The curve $I_{hub}(x)$ was drawn from the standard deviation image calculated over 1000 snapshots in the time history of the visualizations of the wake evolution, analogous to the case of the tip vortices.

The dependence of the instability transition point on the advance ratio is shown in figure 10.

Unfortunately, only two points, limited to $J=0.45$ and $J=0.55$, are available in figure 10 for the two-bladed propeller, the transition occurring downstream of the last optically accessible site in the test section at the higher values of the advance coefficient. The experimental points in figure 10 are best fitted by a linear regression for both the cases of the tip (solid lines) and the hub (dashed lines) vortices.

The analysis points out that the transition to the instability of the tip and hub vortices does not occur simultaneously, independently of the blade number and the propeller loading conditions. This suggests a possible cause–effect relation between the destabilization of the tip vortices and that of the hub vortex. More specifically, we hypothesize that the destabilization of the tip vortices might induce a perturbation which makes the hub vortex unstable. Analyses of the instability transition in a ducted propeller (Felli *et al.* 2008), where a vorticity sheet occurs in the place of coherent tip vortices, seem to support this thesis. In fact, in this case, the hub vortex tends to remain stable for a longer distance than a conventional propeller.

The transition-to-instability position moves downstream when the number of blades is reduced owing to the wider and wider spiral-to-spiral distance. This supports the thesis that the mutual interaction between adjacent spirals is at the base of the propeller wake instability.

The slopes of the regression lines in figure 10 differ on changing the blade number and are larger for the hub vortex. It follows that (i) increasing J , the transition-to-instability position moves downstream more and more on the reducing blade number for both the tip and the hub vortices; (ii) the streamwise shift δ_{trans} at which the hub vortex instability follows the destabilization of the tip vortices (i.e. $\delta_{trans}(J^*) = x_{hub^*}(J^*) - x_{tip^*}(J^*)$) increases on the increasing advance ratio ($\partial\delta_{trans}/\partial J > 0$).

A deeper insight into the instability mechanisms of the tip vortices can be achieved by a detailed analysis of the available images. According to the theoretical model of Widnall (1972), the instability of the tip vortex filaments occurs through three modes: (i) a short-wave instability, (ii) a long-wave instability and (iii) a mutual-inductance instability mode. An exhaustive description of the aforementioned instability modes is given in Widnall (1972).

In practice, the different instability modes are superimposed and, hence, it is rather difficult to isolate them experimentally through visualizations.

The short-wave instability is induced by the self-induced motion of a curved filament in which the local deformation is dominated by the inductance from the nearest points of the filament. Analogous to the wave instability of a vortex ring (Saffman 1970), the short-wave instability is recognizable as a ‘smooth-sinuuous-wave-type’ mode. An example of such an instability mode is given in figure 11, where a short-wavelength sinuous wave is found out in the cavitating trace of the tip vortex.

The mutual-inductance instability mode appears when adjacent helical filaments pass within a distance so that they experience the influence of each other (Widnall 1972). This mutual-inductance effect causes the adjacent spirals to roll-up around each other, resulting in the classic ‘leapfrogging’ phenomenon, often seen with parallel vortex rings (Lugt 1996). A detailed description of such an instability mode is given in figure 12, for $Z = 4$: (i) filaments 1 and 2 begin with the same radius; (ii) under the effect of the mutually induced velocities, filament 1 (back filament) is pulled forward through filament 2 (front filament), reducing its radius as it moves; (iii) meanwhile, filament 2 expands; (iv) the result is that the role of the filaments is reversed and the process may repeat itself.

According to the results of Leishman *et al.* (2002), the mechanism of mutual interaction occurs through a 180° out-of-phase between the axial and radial deformation modes of adjacent tip vortices. In this regard, figure 13 shows the perturbed (cavitating trace) and equilibrium (dashed line) geometries of the tip vortex for the cases of the two- and three-bladed propellers. Geometries of the perturbed tip vortices in the axial direction resemble the characteristic shape of the axial modes 1

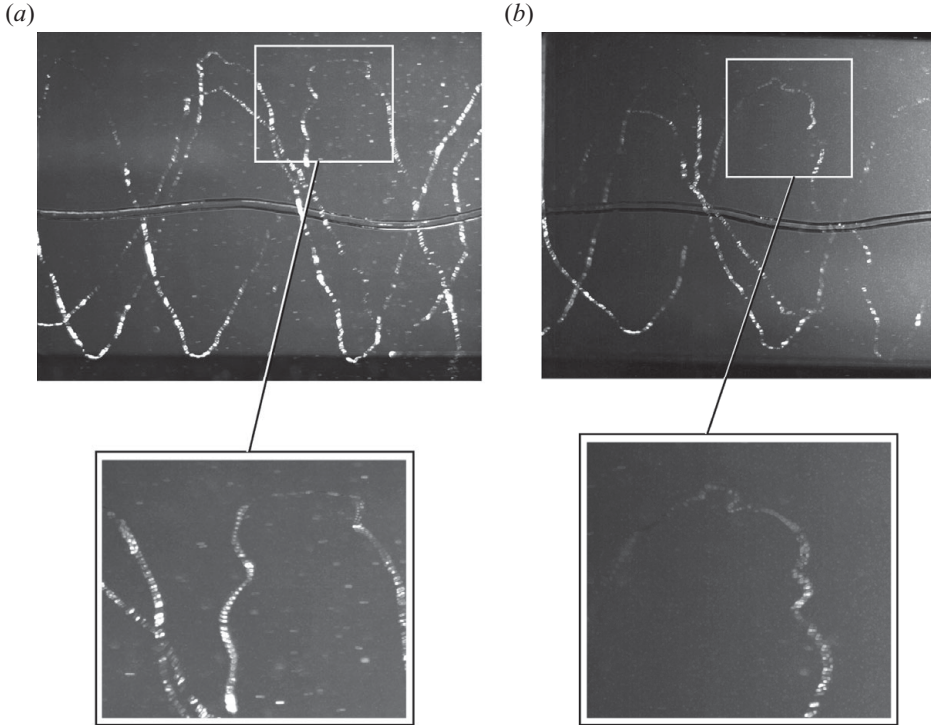


FIGURE 11. Visualizations of the short-wave instability: side (a) and top views (b).

(two-bladed propeller) and 2 (four-bladed propeller). This result is in agreement with the conclusions given in Leishman *et al.* (2002), in which the most unstable modes in a system of Z helicoidal vortices ($Z =$ blade number) are shown to correspond to half-integer multiples of the number of blades.

Figure 14 shows the equilibrium values of the helicoidal pitch τ against the advance ratio J and the blade number Z . Here, the pitch is given by $\tau = h/2\pi a$, where h represents the geometric pitch of a given tip vortex before destabilizing and a the radius of the circumference that surrounds it.

The equilibrium values of the pitch fall outside the stability limits determined by Okulov (2004), for a system of multiple, azimuthally even-spaced helical vortices, and Okulov & Sørensen (2007), limited to the system of N tip vortices of strength Γ and a root vortex of strength $-N\Lambda$ (i.e. Joukowski's model), which results in even more unconditional instability.

The disagreement between the analytical results and the visualization of stable tip vortices on a long distance behind the propeller highlights the ineffectiveness of the above models for predicting stability boundaries of the propeller wake. In this regard, we agree with the assertion of Okulov & Sørensen (2007) that refined models in which the contribution of the trailing vortex sheet is taken into account have to be considered for a more realistic prediction of the stability boundaries of a propeller wake.

In Okulov & Sørensen (2007), the ineffectiveness of the stability models in justifying the occurrence of stable vortices in the near wake of a propeller was overcome by considering multiplicity of helical vortices embedded in an assigned flow field (i.e. Rankine, Gaussian and Scully vortices), representative of the contributions of the

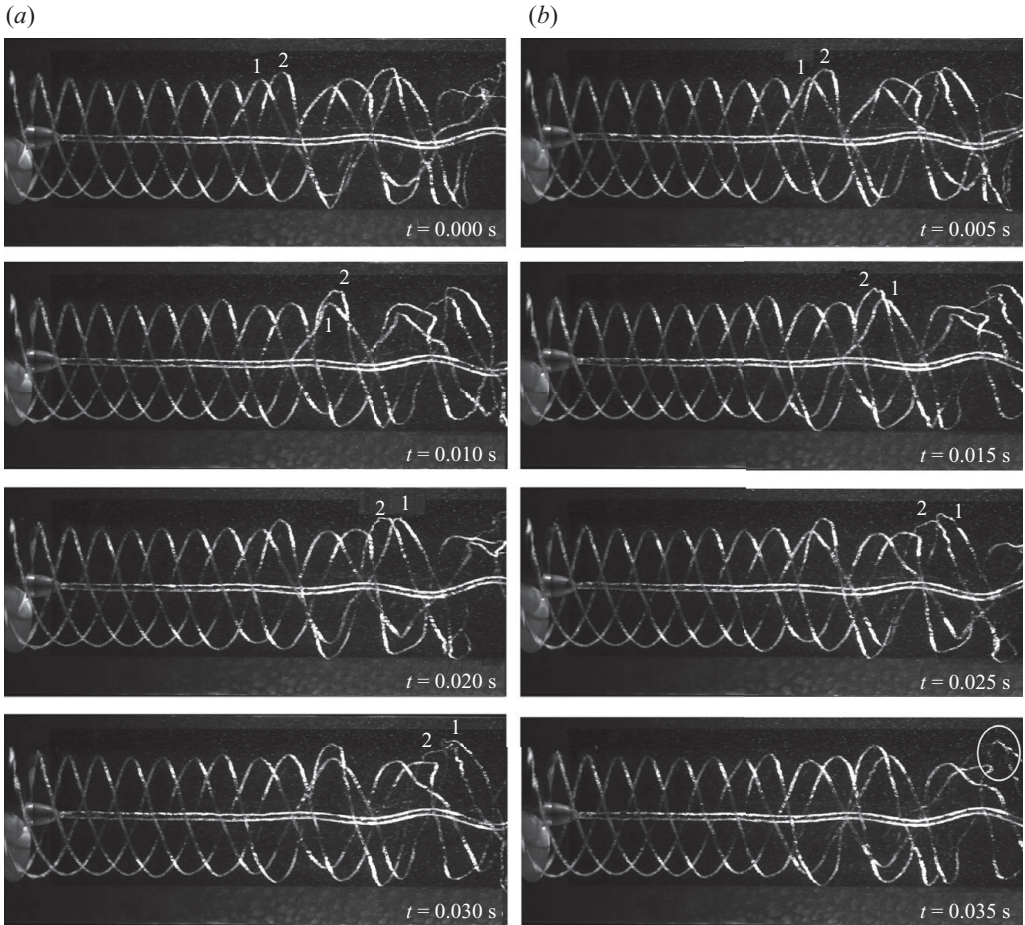


FIGURE 12. (a,b) Mutual inductance between consecutive vortex filaments. Leapfrogging effect between vortices 1 and 2. Snapshots are spaced at $\Delta t = 0.125 T$. Snapshots refer to the case of a four-bladed propeller at $J = 0.65$.

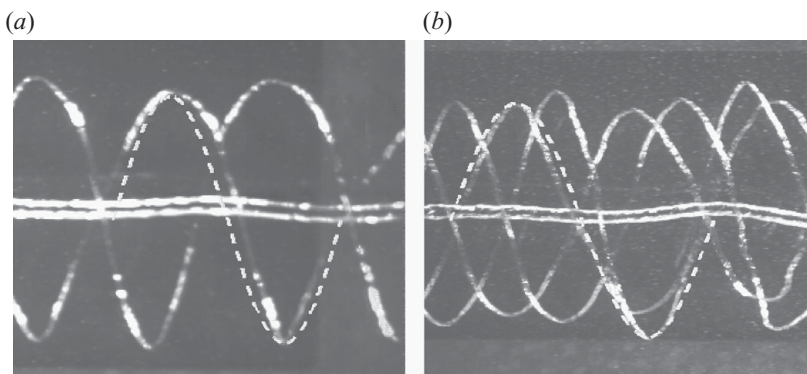


FIGURE 13. Normal-mode perturbations of the tip vortex for $Z = 2$ (a) and $Z = 4$ (b). Dashed lines represent the equilibrium. The tip vortex deformation resembles the shape of mode 1 for $Z = 2$ and mode 2 for $Z = 4$, according to Leishman *et al.* (2002).

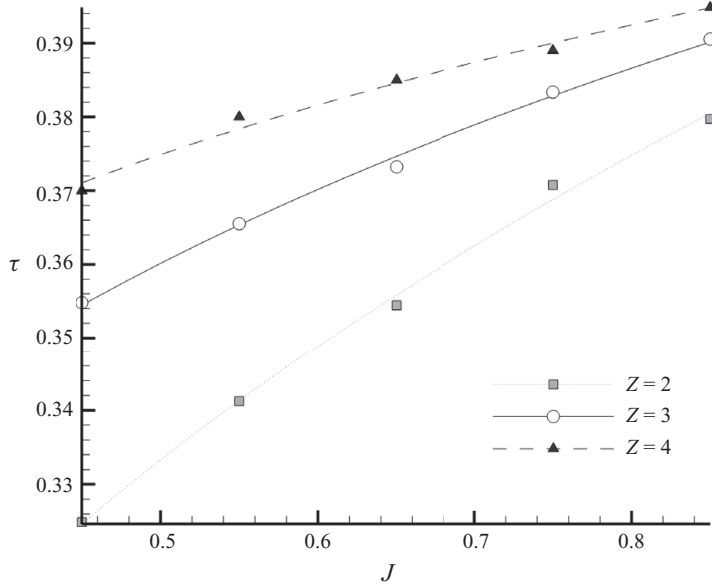


FIGURE 14. Equilibrium pitch of the tip vortex $\tau = h/2\pi a$ against the advance ratio J , for $Z = 2$, $Z = 3$ and $Z = 4$. Pitch was measured considering the cavitating traces of the tip vortices in the visualizations.

trailing wake and the hub vortex. Unfortunately, none of the azimuthally averaged velocity fields derived by the aforementioned assigned vorticity distributions fits with those obtained experimentally for the case of a marine propeller and, thus, it was not possible to refer to those stability boundaries.

In Okulov & Sørensen (2007), it was conjectured that the Joukowski's model becomes valid when the mutual influence between tip vortices and trailing wake is negligible and, thus, concentrated tip vortices are formed. According to the unconditioned instability of the Joukowski's model, in this condition tip vortices destabilize suddenly. The occurrence of concentrated tip vortices is explained to be the consequence of the roll-up process, whose complete development is considered to trigger instability (Okulov & Sørensen 2010).

In the above hypothesis, the transition to instability of propellers having a different number of blades and same intensity of the tip vortex should occur about at the same distance from the propeller plane, the features of the roll-up being correlated mainly to the strength of the tip vortex. This seems to be in contrast with the results of figure 10. Our concern is that the transition to instability may be correlated more to the mutual interference between consecutive spirals than to the complete development of the trailing wake roll-up. In this regard, Di Felice *et al.* (2004) and Felli *et al.* (2006) earlier observed a correlation between the transition to instability of the propeller wake and the interaction between the trailing wake of the actual blade and the tip vortex of the previous one. This interaction induces the tip vortex to lose the link with its trailing wake gradually and definitely, and, thus, to form concentrated tip vortices, such as in the Joukowski model. This aspect is worth discussing thoroughly in a future study.

The amplification rate of the mutual-inductance instability mode is observed to increase with the propeller loading condition (i.e. decreasing J), as shown in figure 8. We assume this behaviour to be the consequence of the following two reasons: (i) the

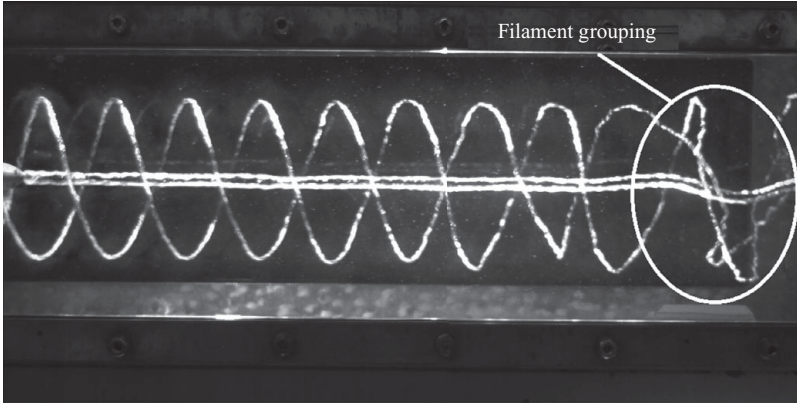


FIGURE 15. Filament grouping for the case of a two-bladed propeller.

reduction of the wake pitch, whose effect on the mutual-inductance mode instability was discussed earlier; (ii) the larger core size of the tip vortex that has a destabilizing effect on the mutual-inductance mode, according to the results by Widnall *et al.* (1972), Okulov (2004) and Okulov & Sørensen (2007).

The analysis of the results achieved at different Z shows that the evolution of the tip vortex filaments occurs through a ‘multi-step’ grouping mechanism, whose characteristics depend on the blade number. More specifically as follows.

(i) The two-bladed propeller ($Z=2$) undergoes only one grouping process that occurs far downstream as for configurations with a larger number of blades; the larger the distance between adjacent spirals, less effective is the destabilizing effect of the mutual inductance (figure 15).

(ii) In the case of the three-bladed propeller ($Z=3$), the grouping mechanism is observed to occur through a two-step process. In the first step, an alternative grouping with one single and one pair of vortex filaments occurs (figure 16*a, b*). More downstream, a complex ‘three-partners-one-single-one-pair’ leapfrogging is observed to occur, in which the single filament tends to be rolled up by the inductance effect of the filaments pair, while progressing in a second grouping with three filaments (figure 16*c, d*).

(iii) In the case of the four-bladed propeller ($Z=4$), the grouping mechanism is analogous to the previous one but the first grouping occurs to form two pairs of filaments and the second step is featured by a ‘four-partner two pairs’ leapfrogging (figure 17).

The analysis of the two-, three- and four-bladed propeller configurations suggests the following equation to describe the dependence of the grouping steps on the blade number:

$$N = \text{ceil}(\log_2 Z), \quad (4.3)$$

where N is the number of grouping steps, Z is the blade number ($Z=2, 3, 4$) and $\text{ceil}(A)$ is a function that rounds A to the nearest integer greater than or equal to A . The validity of (4.1) was verified for the case of the E779a propeller geometry limited to the two-, three- and four-blade configurations. Further tests performed on different propellers with five and six blades seem to confirm (4.1), even though the extension to a general content is still to be demonstrated.

The general features of the hub vortex instability are highlighted in figures 18–20. The following aspects can be pointed out.

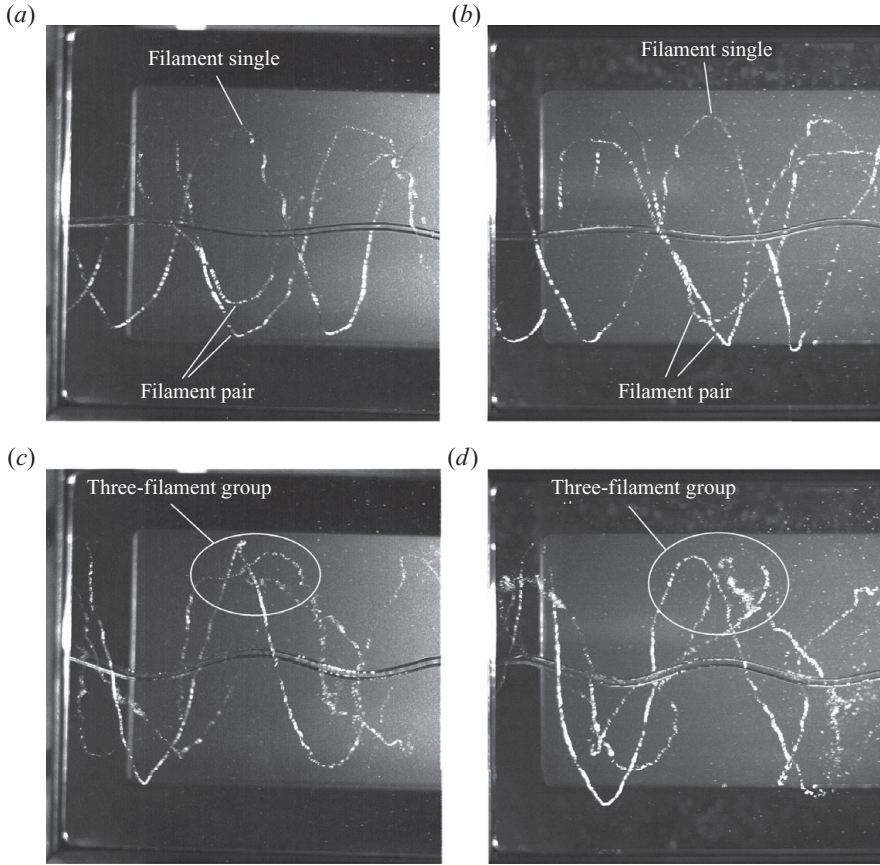


FIGURE 16. First (*a, b*) and second (*c, d*) grouping steps for the case of a three-bladed propeller. *XZ* (*a, c*) and *XY* views (*b, d*) at the same instant.

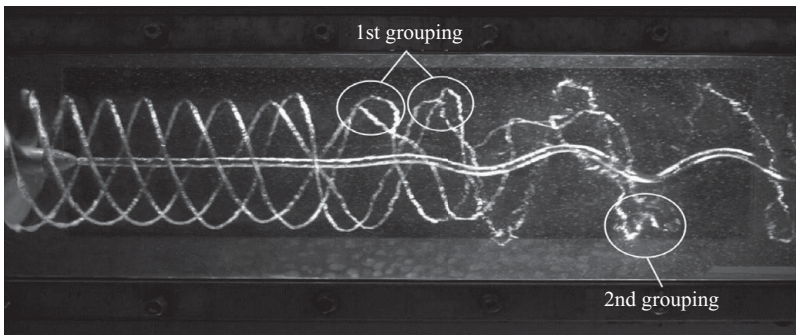


FIGURE 17. Grouping steps for the case of a four-bladed propeller.

(i) At the transition point the hub vortex starts to oscillate according to a spiral geometry until breakdown occurs.

(ii) The period of the hub vortex oscillation equals that of one propeller revolution T and, thus, it is independent of the blade number and the advance ratio. This results from the analysis of the cavitating trace of the hub vortex that recurs periodically with a period $\Delta t = T$ (figures 18–20).

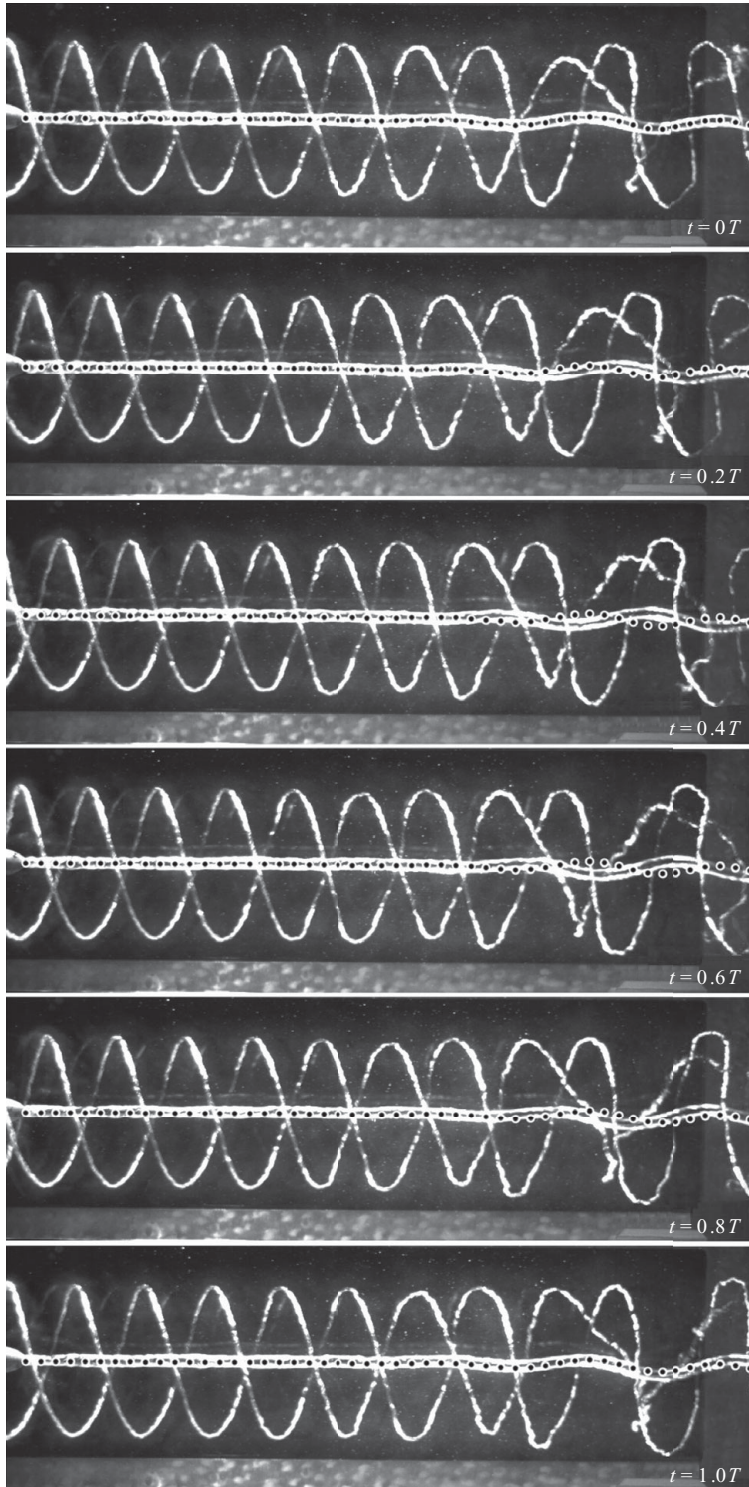


FIGURE 18. Hub vortex evolution for the case of a two-bladed propeller. Dots represent the cavitating trace of the hub vortex at $t = 0$. The traces of the hub vortex appear aligned after a revolution period of the propeller.

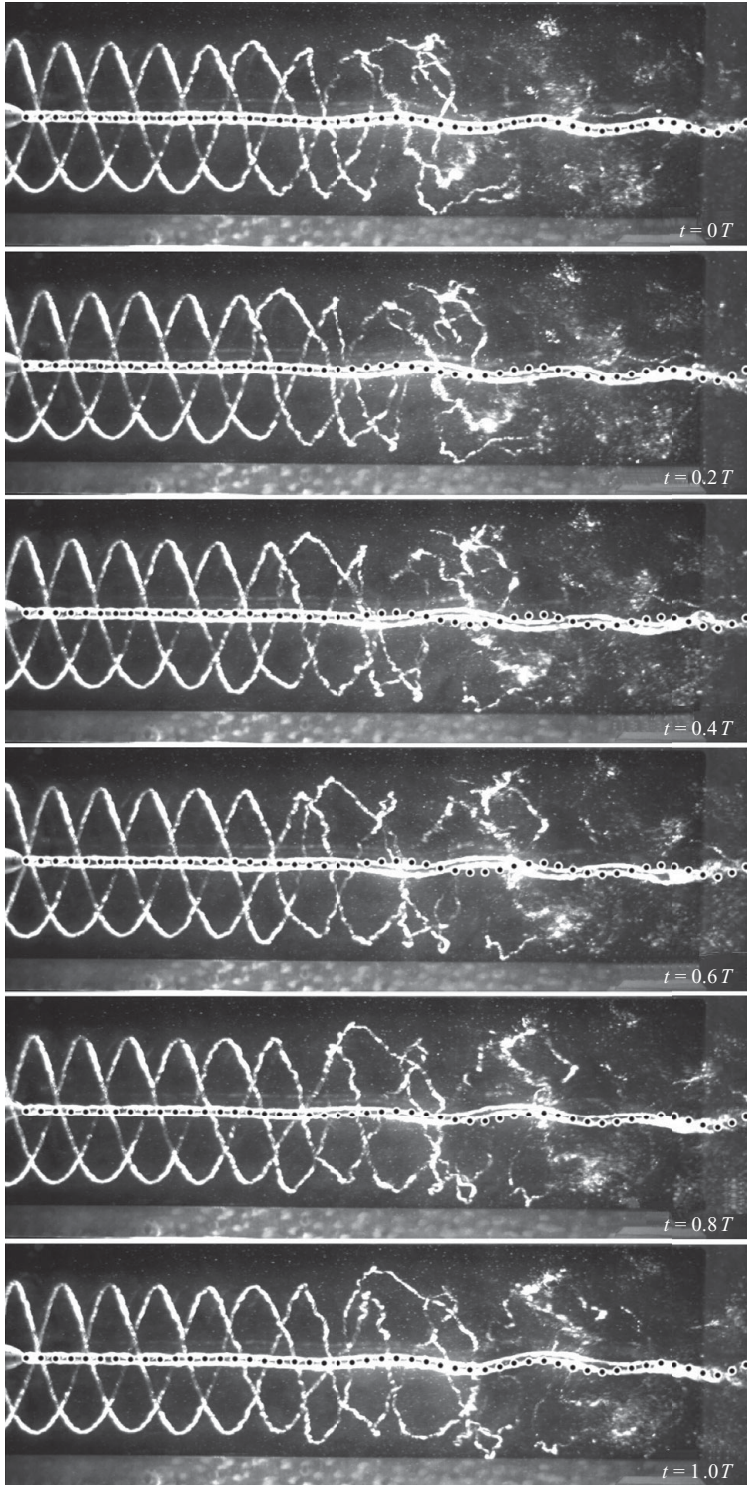


FIGURE 19. Hub vortex evolution for the case of a three-bladed propeller. Dots represent the cavitating trace of the hub vortex at $t=0$. The traces of the hub vortex appear aligned after a revolution period of the propeller.

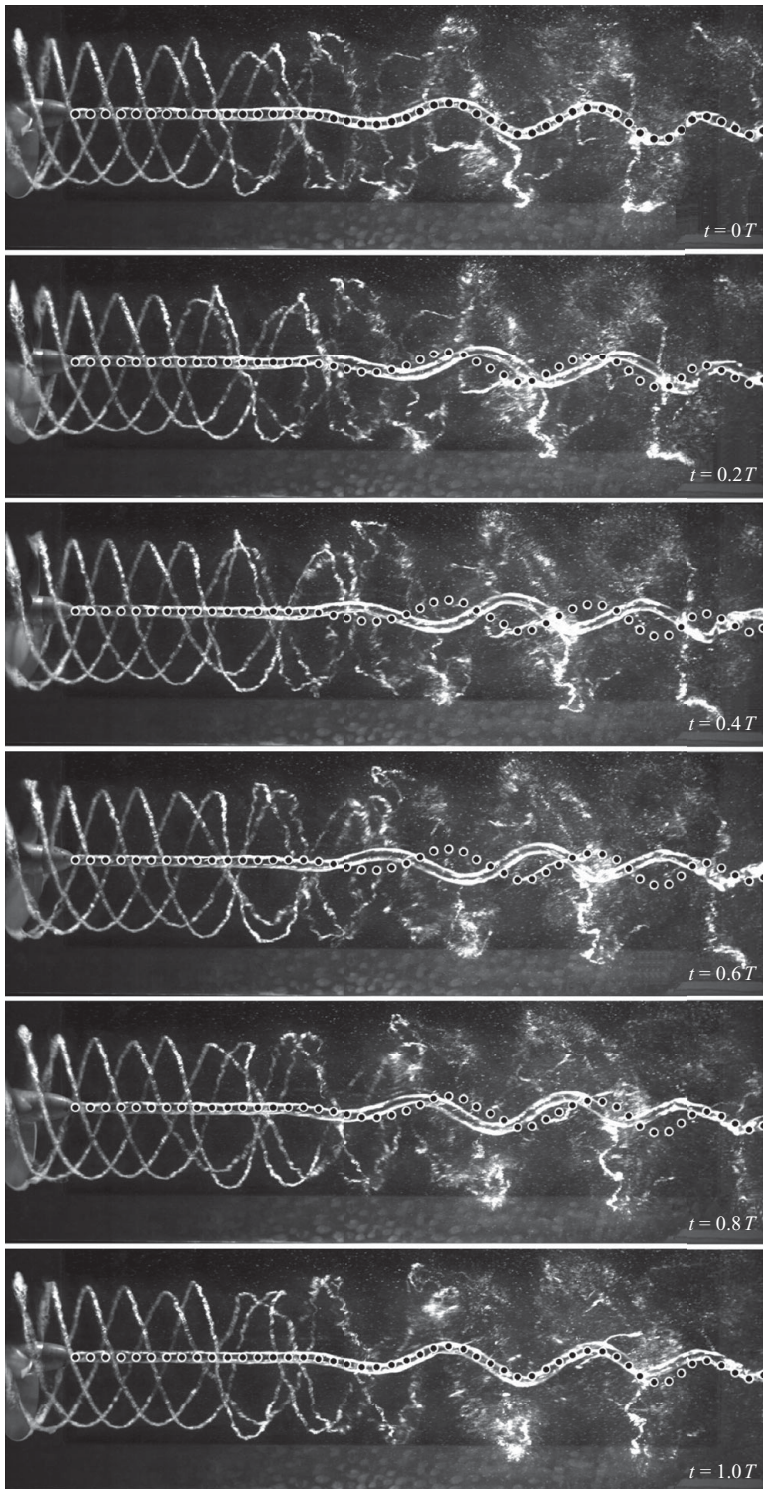


FIGURE 20. Hub vortex evolution for the case of a four-bladed propeller. Dots represent the cavitating trace of the hub vortex at $t = 0$. The traces of the hub vortex appear aligned after a revolution period of the propeller.

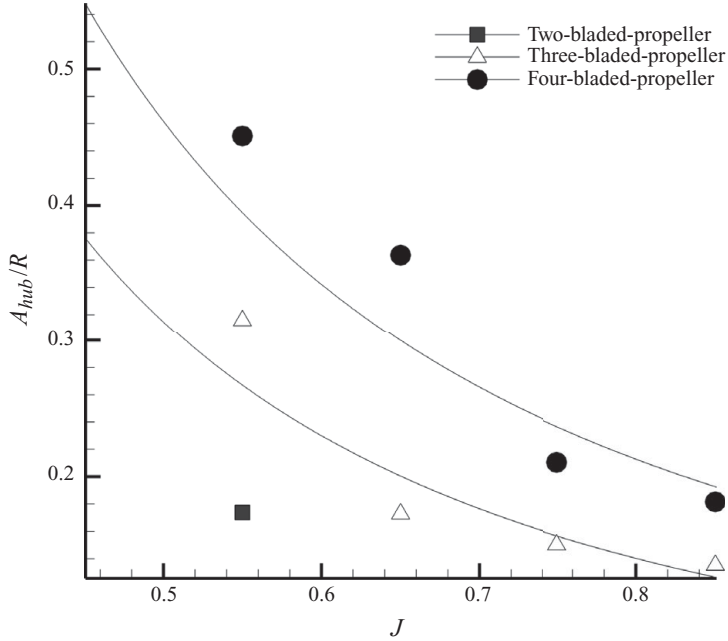


FIGURE 21. Oscillation amplitude of the hub vortex versus the advance coefficient for $Z = 2$, $Z = 3$ and $Z = 4$.

(iii) The amplitude of the hub vortex oscillation shows dependence on the propeller loading conditions and, thus, on the advance coefficient J . Graphs in figure 21, describing the maximum amplitude of the hub vortex oscillation versus the advance coefficient for different Z , seem to support the conjecture that the number of helices in a propeller wake influences the amplitude of the hub vortex oscillation, besides having an effect on the position where the hub vortex destabilizes. The oscillation amplitude is observed to reduce on increasing the advance coefficient.

4.1.2. Propeller far-wake evolution and breakdown

A qualitative analysis of the far-wake evolution and breakdown was performed on the basis of a number of time-resolved visualizations performed at different values of the advance coefficient J and the blade number Z .

In the far wake the cavitating traces of the tip vortices appear distorted and more and more weaker as the distance from the propeller increases, the latter due to the diffusion of vorticity that accomplishes the mutual interaction among tip filaments and, thus, by a more and more flat profile of low pressure in the vortex core that reduces the amount of cavitation.

In the far wake, the hub vortex undergoes progressive deformation until breakdown occurs.

Figures 22 and 23 show a complex interaction between the hub vortex and the tip filaments that occurs in the far wake of the three- and four-bladed propellers. This interaction occurs following a mechanism similar to that documented in Klein, Majda & Damodaran (1995) and Ortega, Bristol & Savaş (2003). More specifically, the tip vortex filaments tend to be rolled up and collide with the hub vortex, owing to the inductance of the latter. This interaction stresses the hub vortex, causing its sudden destabilization.

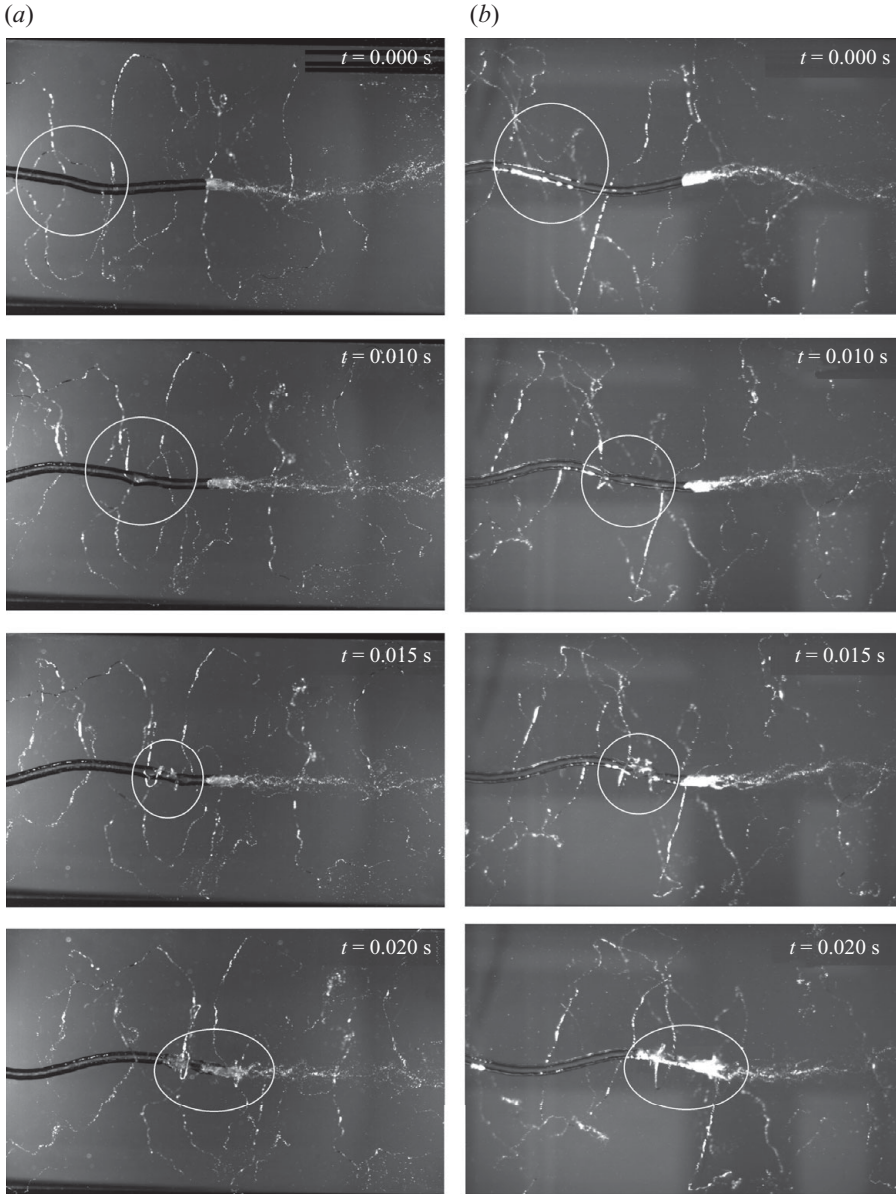


FIGURE 22. Far-wake evolution of the three-bladed propeller: roll-up of a tip vortex around the hub vortex. XZ (a) and XY (b) views. Snapshots are spaced at $\Delta t = 0.125 T$.

The key parameters that drive this phenomenon are the distance and the relative circulation between the hub vortex and a single tip vortex filament. According to the definition given in Klein *et al.* (1995), the relative circulation is here defined as

$$\Gamma = \frac{\Gamma_{hub}}{\Gamma_{tip}}, \quad (4.4)$$

where Γ_{tip} and Γ_{hub} are the circulation values of the tip and the hub vortex, respectively.

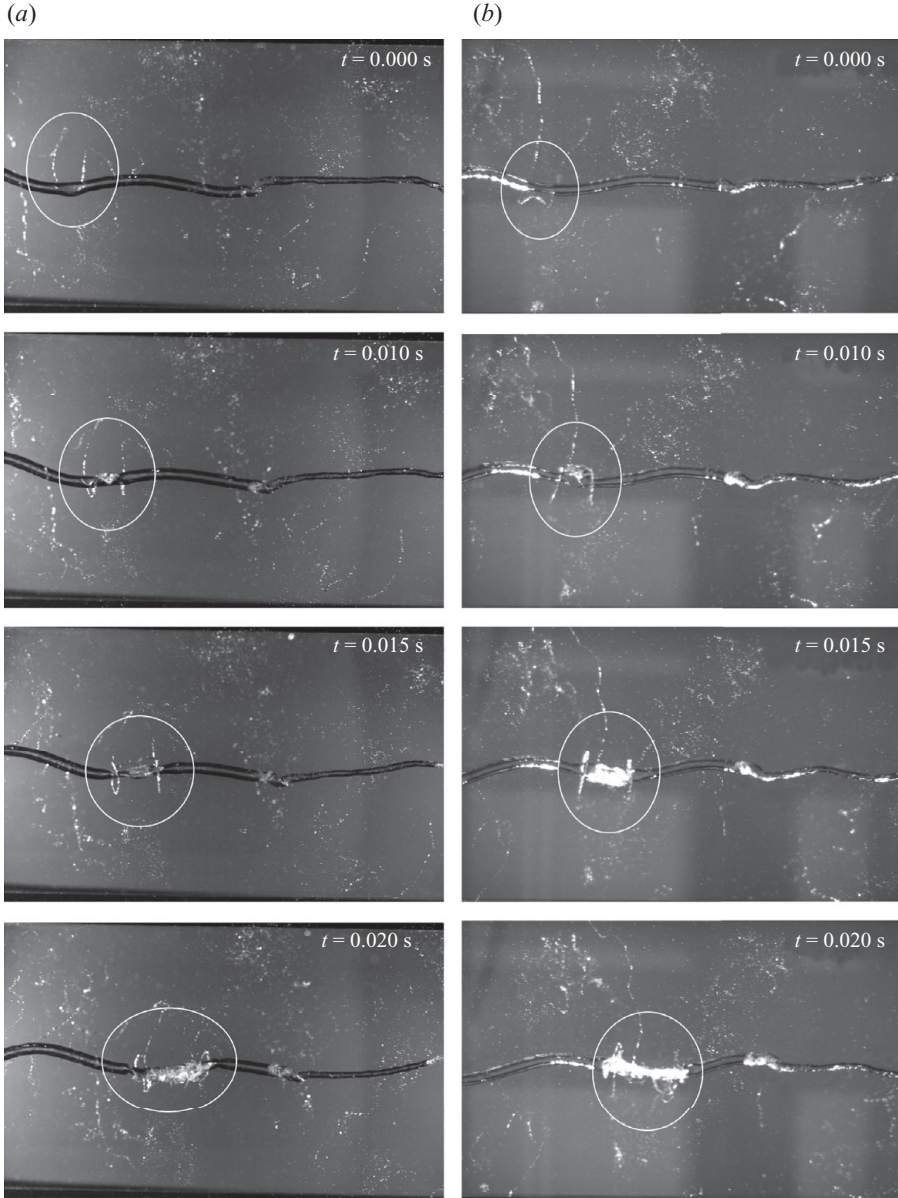


FIGURE 23. Far-wake evolution of the four-bladed propeller: roll-up of a tip vortex around the hub vortex. XZ (a) and XY (b) views. Snapshots are spaced at $\Delta t = 0.125T$.

In the far wake of a propeller, the above interaction appears as a random event at first sight. The dynamical analysis in §4.2 supports this thesis showing more and more chaotic behaviour of the tip vortices in the far wake.

Therefore, in the chaotic dynamics of the tip vortex, it is statistically possible that it might pass under the region of influence of the hub vortex and interact with it. It is reasonable to think that the probability of such an interaction increases with the circulation ratio Γ and reduction in the inter-distance.

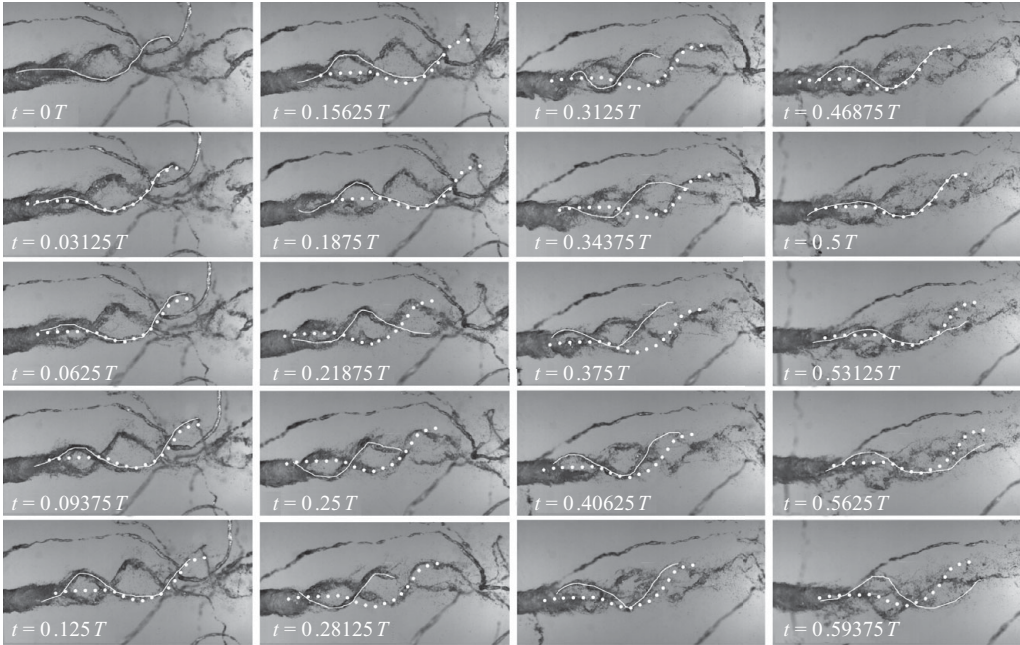


FIGURE 24. Double-helix breakdown for the two-bladed propeller. Dotted lines represent the cavitating traces of the reference filament of the double helix at $t=0$, and solid lines represent the current cavitating traces of the reference filament of the double helix. The best alignment between dotted and solid lines appears after about $\Delta t = T/2$.

The absence of evidence of this induction effect in the case of the two-bladed propeller regardless of the loading conditions seems to confirm this conjecture.

For the $z > 2$ cases, the distance at which the hub vortex inductance is effective increases with Γ . This explains the larger number of interaction events observed in the visualizations when Z was increased.

The hub vortex breakdown appears as a double helix (Sarpkaya 1971) that evolves by shearing and splitting of the centreline filament maintaining the same sense of rotation as the propeller. This is shown in the visualizations of figures 24–26, where the time history of the cavitating traces of the double helix is shown for $Z = 2$, $Z = 3$ and $Z = 4$.

The analysis of the characteristic frequency of the double-helix rotation was performed by imaging the breakdown region and comparing the current cavitating trace of a reference filament with its trace at $t = 0$ (figures 24–26). The result shows that the oscillation period of the double helix T_{break} equals that of the blade passage (i.e. $T_{break} = T/Z$) independent of the blade number.

In all the analysed conditions (i.e. different J and Z), the position of the hub vortex breakdown was observed to fluctuate up and down, ranging within a region whose extent is observed to become larger and larger for increasing J . We assume this behaviour to be the consequence of fluctuations in the downstream flow (in the sense of Sarpkaya 1971) whose intensities increase on the increasing loading condition (i.e. reducing J) and whose effect is to cause upstream (flow deceleration) and downstream (flow acceleration) movements of the breakdown position, according to Sarpkaya (1971).

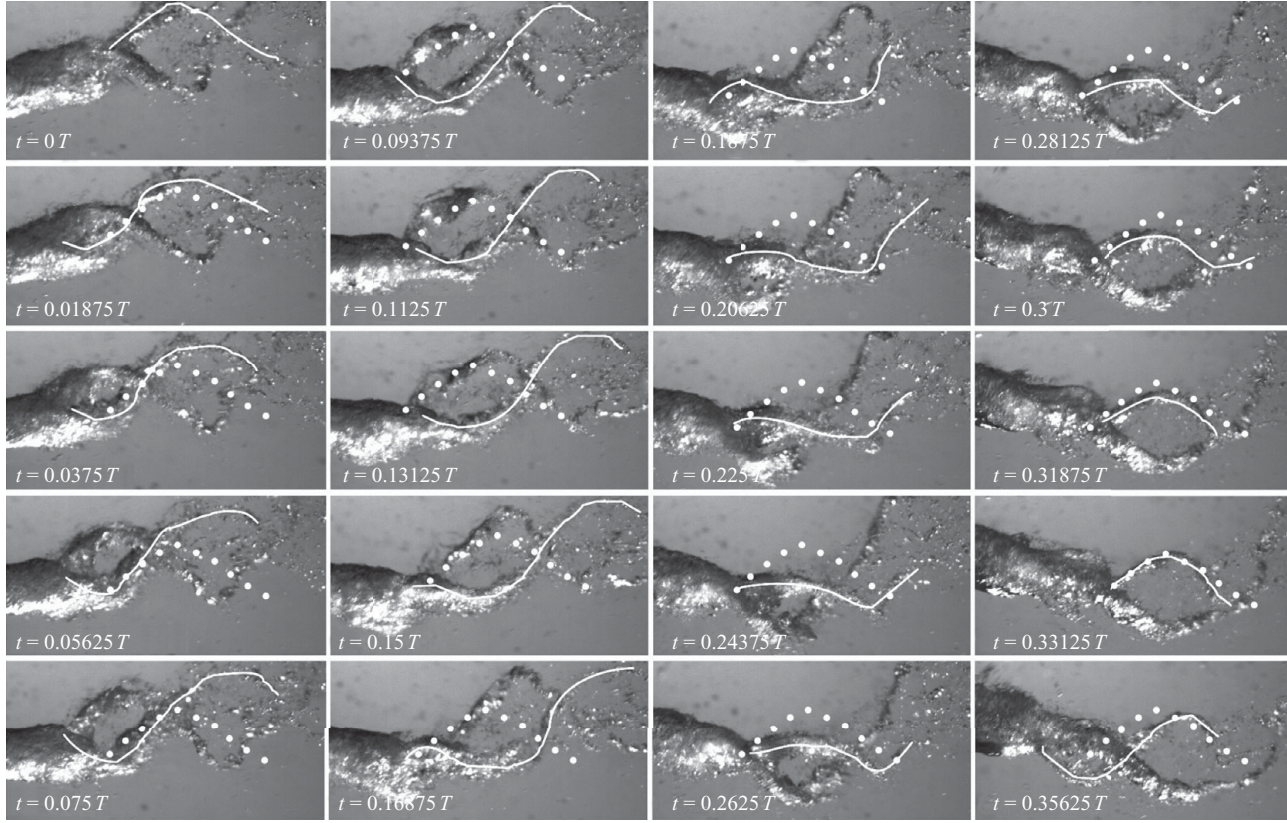


FIGURE 25. Double-helix breakdown for the three-bladed propeller. Dotted lines represent the cavitating traces of the reference filament of the double helix at $t=0$, and solid lines represent the current cavitating traces of the reference filament of the double helix. The best alignment between dotted and solid lines appears after about $\Delta t = T/3$.



FIGURE 26. Double-helix breakdown for the four-bladed propeller. Dotted lines represent the cavitating traces of the reference filament of the double helix at $t = 0$, and solid lines represent the current cavitating traces of the reference filament of the double helix. The best alignment between dotted and solid lines appears after about $\Delta t = T/4$.

4.2. Dynamical analysis

4.2.1. Test matrix and conditions

In the present paper, the dynamical analysis was focused on investigating the effect of the spiral-to-spiral distance and the blade number on the evolution mechanisms of the tip vortices. In this regard, with the scope of eliminating the dependence upon the vortex strength, the advance ratio of each propeller was adjusted in order to obtain the same tip vortex intensity.

It is worth pointing out that even the hydrodynamic pitch of the wake shows dependence on the advance ratio (Di Felice 2004). However, this effect can be reasonably considered of secondary importance compared to that of the different spiral-to-spiral distances when the blade number is varied (Okulov 2004).

The actual configurations adopted in the experiments for the three propellers were determined through a preliminary numerical analysis. Specifically, advance ratio values giving the same tip vortex intensity in the three propellers were determined through an inviscid irrotational flow model (Greco *et al.* 2004). The intensity of the blade-shed vorticity was determined as $d\Gamma/ds$, where Γ is circulation and derivation is taken along a path lying on the shed vortex sheet and normal to vortex lines. Here, an estimate of the tip vortex strength is determined by calculating the spanwise

Blade number (Z)	N (r.p.s.)	U_∞ (m s ⁻¹)	Corrected advance ratio (J)	Advance ratio (J)	Reynolds number (Re)
2	25	4.54	0.8	0.794	1.141×10^6
3	25	4.26	0.75	0.745	1.133×10^6
4	25	4.03	0.71	0.705	1.127×10^6

TABLE 2. Test conditions of the LDV measurements.

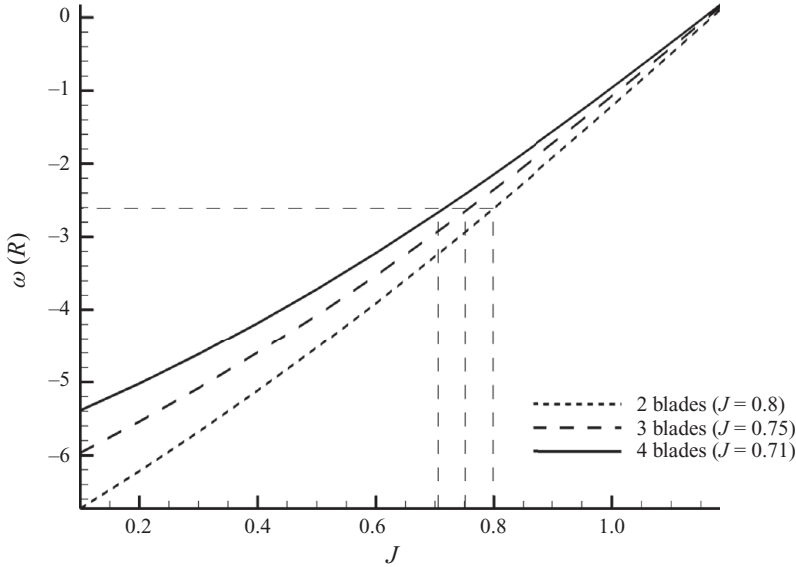


FIGURE 27. Tip vortex intensity as a function of the advance ratio for the two-, three- and four-bladed propeller models

derivative of circulation Γ at the blade tip, as

$$\omega(R) = \frac{\partial \Gamma(R)}{\partial s}, \quad (4.5)$$

where s is the arclength along the blade's trailing edge. The derivation of the circulation should have been taken along a path lying on the shed vortex sheet and normal to vortex lines. However, propeller blades have a typically complex geometry and the radial direction is a rough approximation of such a shedding line. For this reason, the partial derivative has been taken with respect to the trailing edge, which was proved to provide a better description of the shedding line.

The graph in figure 27 compares tip vortex intensities from the above equation for two-, three- and four-bladed propellers against the advance ratio.

Assuming the two-blade configuration at $J = 0.8$ as a reference, the corresponding values of the advance ratios for the three- and four-bladed propellers were $J = 0.75$ and $J = 0.71$, respectively.

The experimental conditions investigated through the dynamical analysis are documented in table 2, where the values of the advance ratio are adjusted to account for the tunnel effect. For the sake of completeness, the values of the advance coefficients before the correction are also reported in table 2. The differences in the

Blade number (Z)	Corrected advance ratio (J)	Γ_{tip} ($\text{m}^2 \text{s}^{-1}$)	Γ_{hub} ($\text{m}^2 \text{s}^{-1}$)	γ
2	0.8	0.0725	-0.173	-1.19
3	0.75	0.0722	-0.321	-1.48
4	0.71	0.0728	-0.479	-1.64

TABLE 3. Strength of the tip and hub vortices and circulation ratio of the three propeller configurations in the LDV measurements.

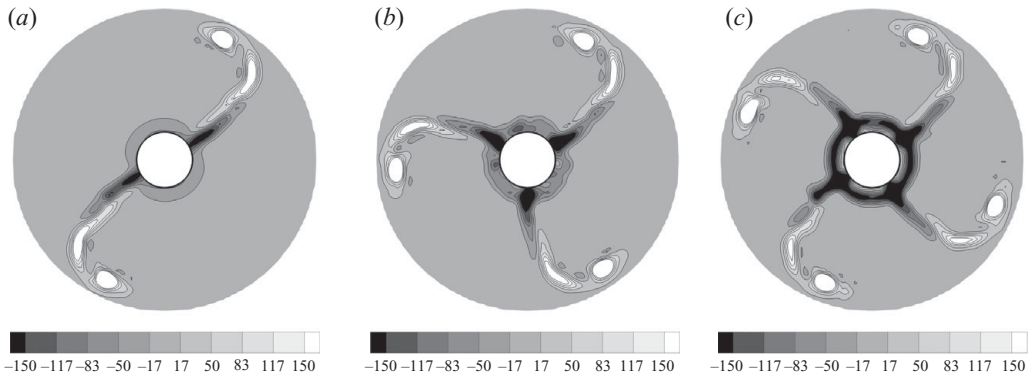


FIGURE 28. Normalized vorticity field for the two- (a), three- (b) and four- (c) bladed propellers at $J=0.8$, $J=0.75$ and $J=0.71$, respectively. In the three propellers, the intensity of the tip vortices is the same according to the results of figure 24.

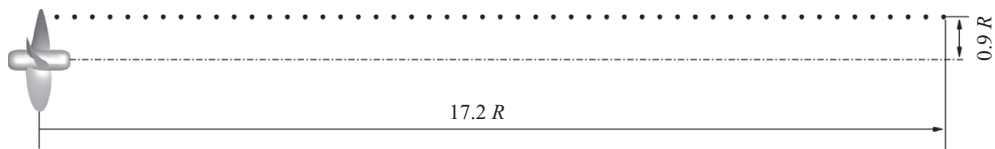


FIGURE 29. Measurement grid used for the dynamical analysis of the tip vortices.

Reynolds numbers among the three configurations are negligible, as documented in table 2.

The results of figure 27 were verified experimentally through LDV measurements providing the velocity field along a transversal section of the wake just behind the blade's trailing edge. In this regard, figure 28 shows the distribution of the axial vorticity at the test conditions specified above: the circulation at the blade tip confirms that the tip vortex intensity is constant regardless of the different propeller configurations. This result is supported by table 3, in which the circulation of the tip and hub vortices and the circulation ratio $\gamma = \Gamma_{hub} / N \Gamma_{tip}$, measured by LDV, are reported for the three propeller configurations.

The analysis was carried out considering LDV velocity signals acquired along a grid of 50 equi-spaced points that extends longitudinally from the propeller trailing edge up to about $x = 17R$ downstream (figure 29). Velocity signals were acquired at the mean data rate of about 1 kHz and the acquisition time was 600 s point⁻¹.

4.2.2. Results of the dynamical analysis

The study of the dynamical behaviour of the tip vortex system was carried out by applying the mathematical tools described in §3 to the velocity signals acquired at different streamwise positions of the wake (figure 29).

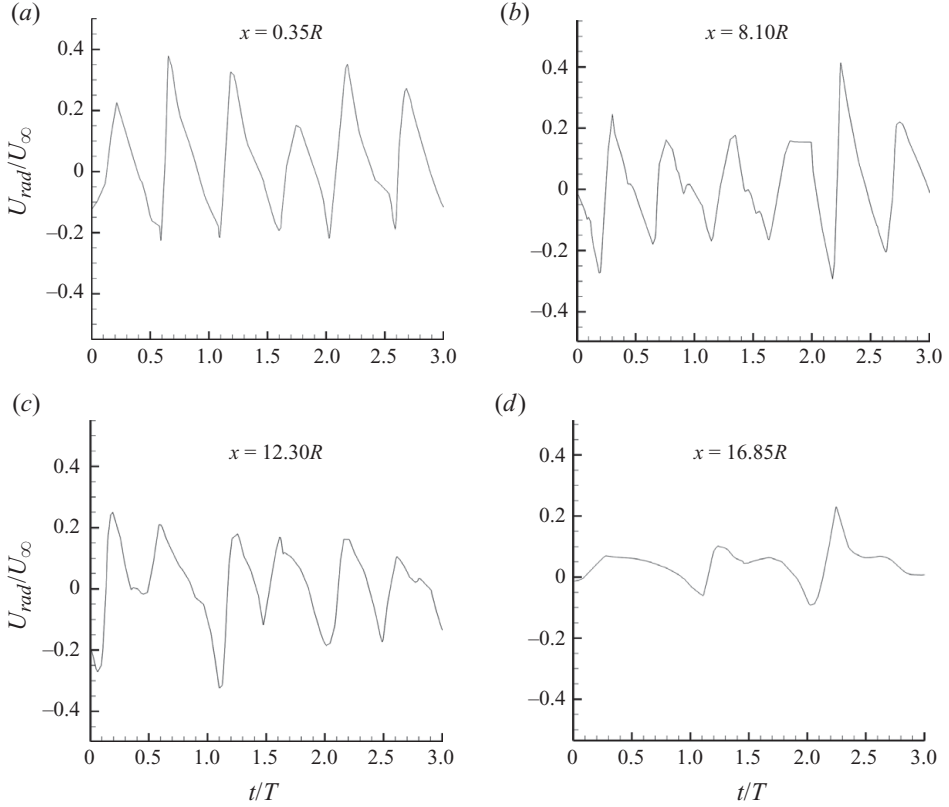


FIGURE 30. Two-bladed propeller. Time history of the radial velocity (U_{rad}). Velocities are normalized with the free-stream velocity ($U_{[inf]}$).

The analysis aims at providing a deeper insight into the evolution mechanisms of the tip vortices in the transition and the far field, integrating the results of the visualizations described in §4.1.

With reference to the dynamics of the tip vortices, one can identify two regions: (i) the near field in which the tip vortex passage occurs regularly at the blade frequency and (ii) the transition and the far field in which the tip vortices destabilize more and more until breakdown occurs.

The time histories and the phase-averaged evolutions of the velocity signals at different streamwise positions of the tip vortices are reported in figures 30–32 (time history) and figures 33–35 (phase-averaged velocities) for $Z=2$, $Z=3$ and $Z=4$, respectively.

In the near field, the velocity signals show a periodic trend with a periodicity that is correlated to the regular passage of the tip vortices over the measurement volume. It follows that characteristic period of the perturbation is $T_{blade} = Z/n$ s. The occurrence of some nonlinear effects in the time histories of the velocity signals is the consequence of the high level of turbulence in the tip vortex (Chesnaks & Jessup 1998; Stella *et al.* 2000). Such nonlinearities are filtered out when the velocity signals are phase averaged. The extent of the near field ranges from the blade's trailing edge up to a distance that depends on the blade number and, in general, on the advance coefficient (Di Felice *et al.* 2004), as discussed in §4.1.1.

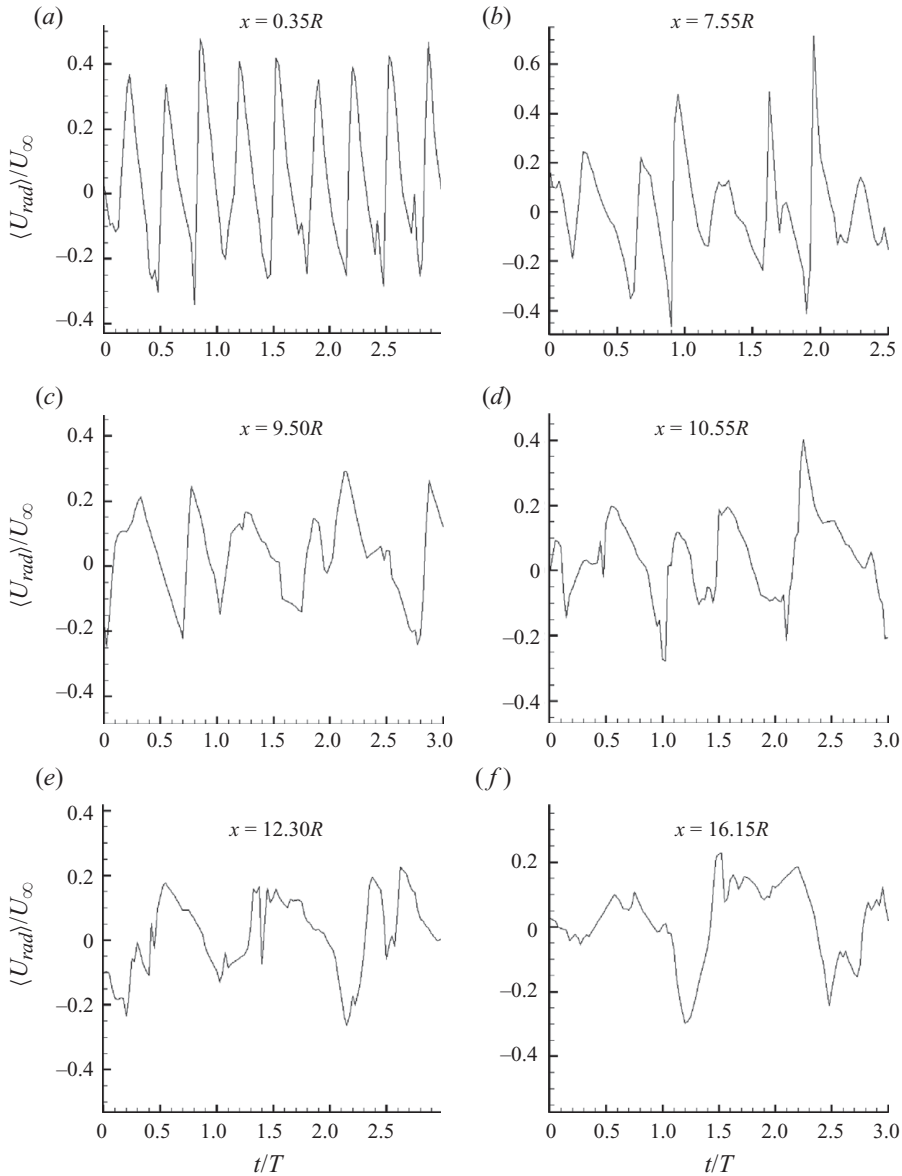


FIGURE 31. (a–f) Three-bladed propeller. Time history of the radial velocity. Velocities are normalized with the free-stream velocity.

Starting from the transition field, the time histories of the velocity signals evidence that a less and less periodic trend is observed when moving streamwise. In this regard, a better understanding of the tip vortex dynamics is given by the phase-averaged velocity signals that highlight a process in which peaks representing the passage of the tip vortices appear less and less even-spaced streamwise till merging further downstream.

This behaviour is further evidence of the mutual-inductance instability mode whose effect reveals through the grouping among adjacent tip vortex filaments, as documented in §4.1.1.

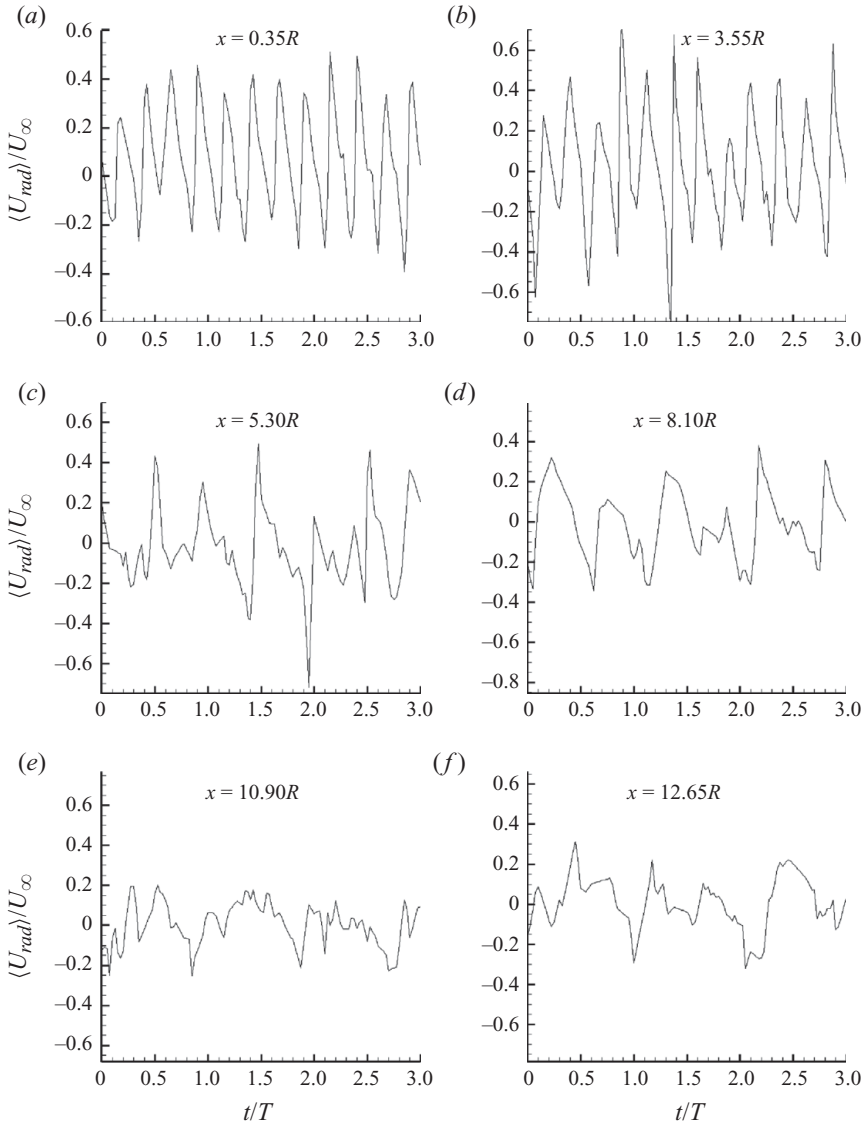


FIGURE 32. (a–f) Four-bladed propeller. Time history of the radial velocity. Velocities are normalized with the free-stream velocity.

More specifically, the following features can be observed by the graphs of figures 33–36, the last figure representing the overview of the streamwise evolution of the phase-averaged velocity:

(i) *Two-bladed propeller*. The peaks of the radial velocity, 180° circumferentially spaced in the near wake (see figure 33a,b), get closer in pairs starting from about $x = 10R$, as highlighted by the gradual reduction of their distance: 170° at $x = 12.30R$ and 160° at $x = 16.85R$. The complete merging of the velocity peaks was not observed in the velocity signals because it occurs downstream of the test section at $J = 0.8$.

(ii) *Three-bladed propeller*. The velocity peaks tend to approach in groups of three. In each group the positions of the peaks are less and less even-spaced with increasing the distance from the propeller: 105° and 135° are the distances between

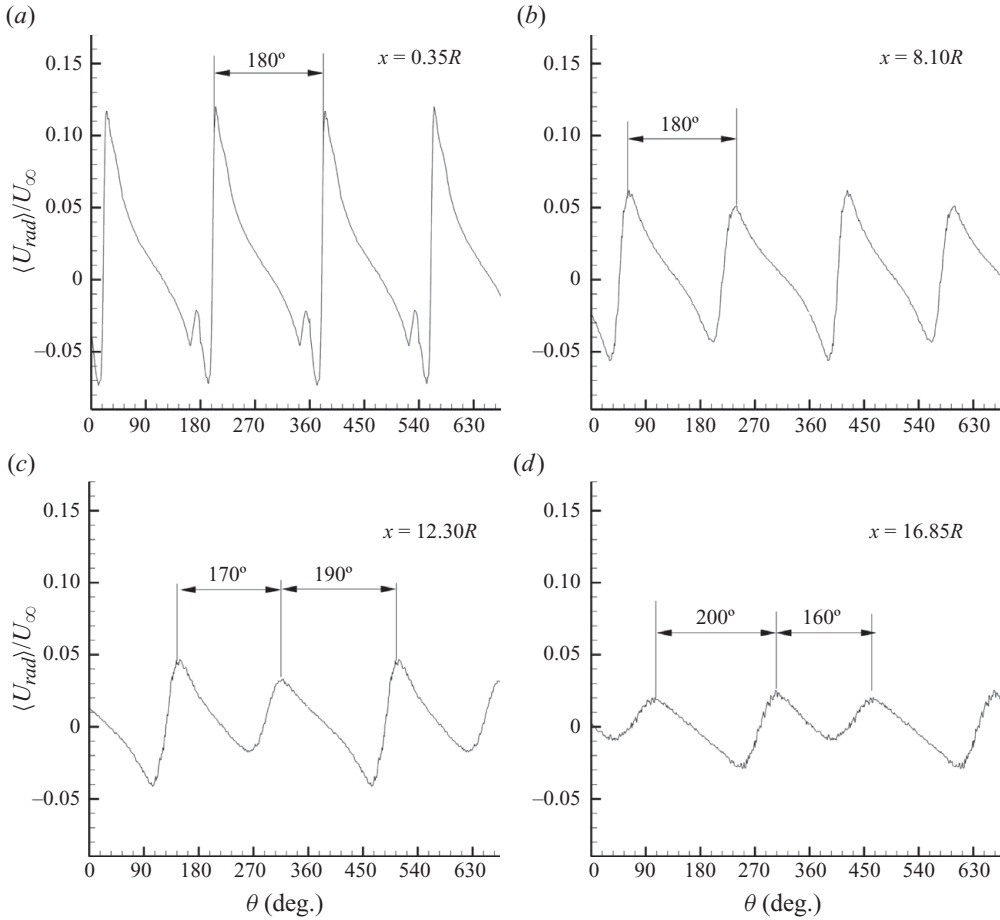


FIGURE 33. (a–d) Two-bladed propeller. Angular evolution of the phase-averaged radial velocity. Velocities are normalized with the free-stream velocity.

consecutive peaks in a group at $x = 7.75R$, 95° and 150° at $x = 9.50R$, 82° and 118° at $x = 10.55R$ (figure 34). Further downstream, at $x = 12.30R$ and $x = 16.15R$, the traces of the velocity peaks completely vanish in each group, replaced by a wider single contribution given by the superposition of the three signals.

(iii) *Four-bladed propeller.* In this case, the grouping mechanism occurs between pairs of velocity peaks, starting from nearly $x = 3R$. Plots at $x = 3.55R$ (figure 35) show a circumferential distance of 80° and 100° between two peaks of the same group and two consecutive groups, respectively. Moving downstream, the trend is a gradual reduction of the peak-to-peak distance inside a group and a gradual increase of the peak-to-peak distance between one group and the other. This process ends around $x = 8R$, resulting in a complete merger between peaks of the same group and a new peak-to-peak distance of about 180° (figure 35d). The second step of the grouping process is already completed at $x = 12.65R$, where the phase-averaged velocity signals show 360° spaced peaks resulting from the merger of the two-filament pairs in a group of four filaments (figure 35f).

A complementary view of the first grouping step is provided by the contour plots of figure 37 that represent the distribution of the axial vorticity (i.e. ω_x) for $Z = 2$, $Z = 3$

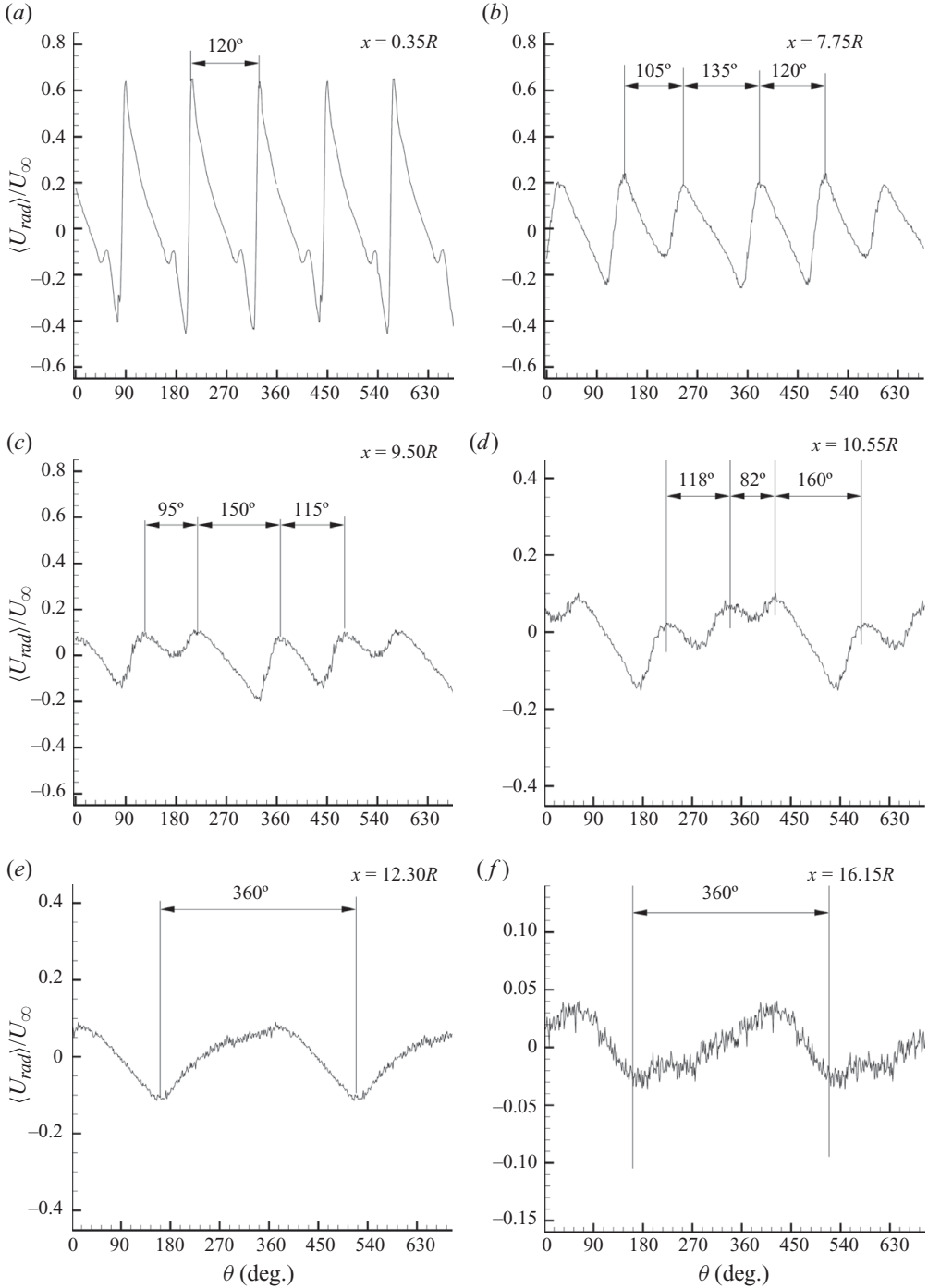


FIGURE 34. (a–f) Three-bladed propeller. Angular evolution of the phase-averaged radial velocity. Velocities are normalized with the free-stream velocity.

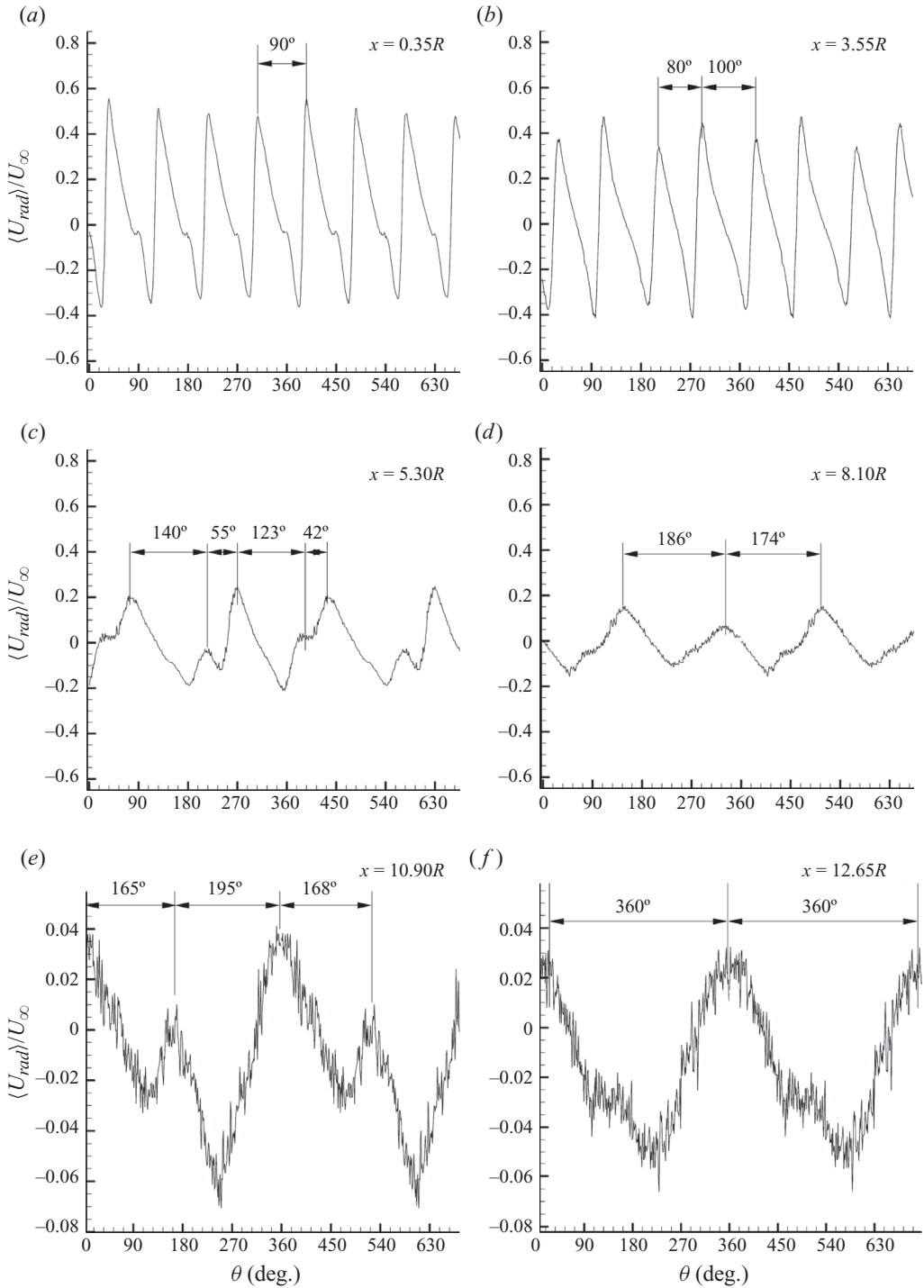


FIGURE 35. (a-f) Four-bladed propeller. Angular evolution of the phase-averaged radial velocity. Velocities are normalized with the free-stream velocity.

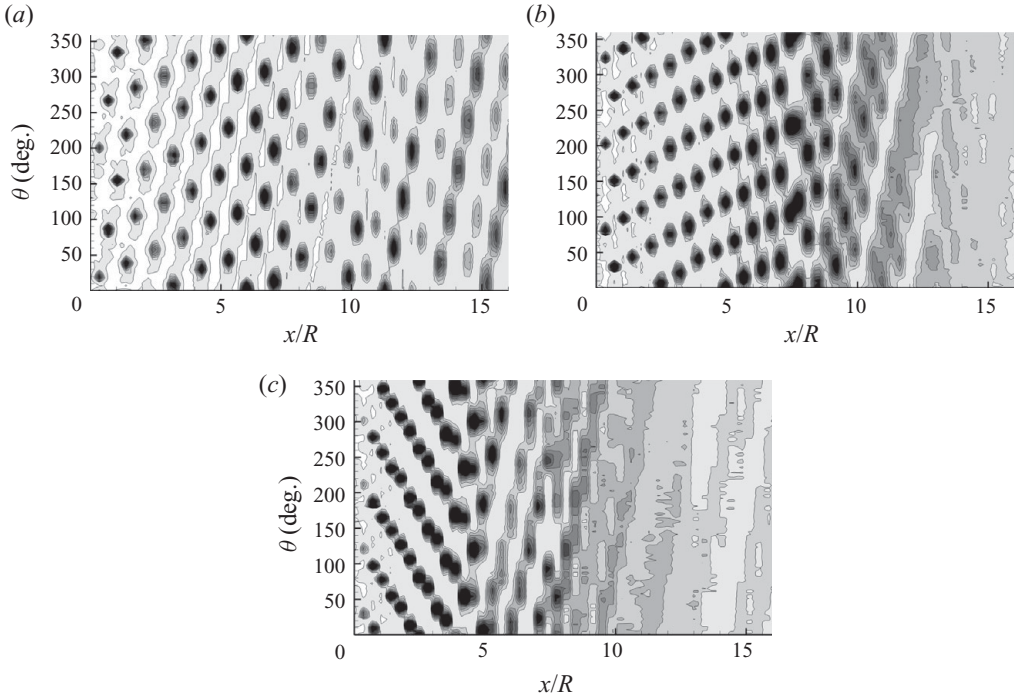


FIGURE 36. Phase-averaged evolution of the tip vortex TKE for the two- (a), three- (b) and four-bladed (c) propellers.

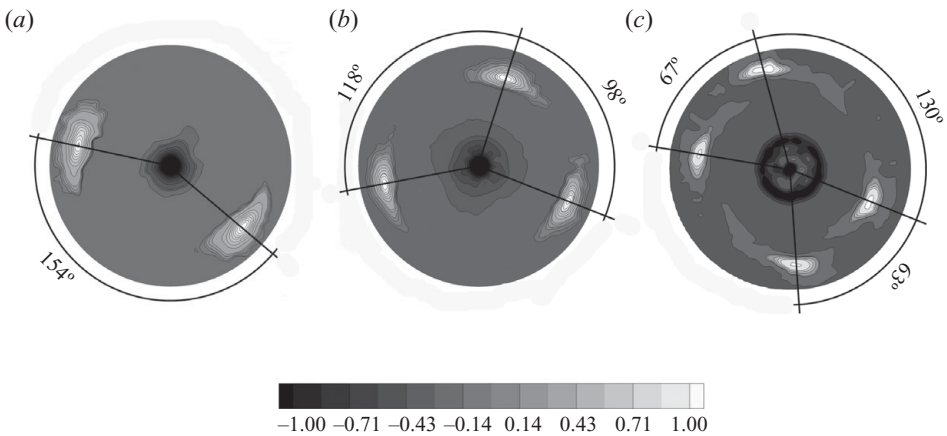


FIGURE 37. First step of the tip vortex grouping mechanism for $Z = 2$ (a), $Z = 3$ (b) and $Z = 4$ (c).

and $Z = 4$ in the transition wake. Here, the traces of the tip vortices are uneven spaced as the consequence of the mutual-inductance effects that tends to group the tip vortex filaments to get a system of one pair ($Z = 2$), one-single one pair ($Z = 3$) and two pairs ($Z = 4$).

Figures 38–40 show the distribution of the normalized power spectrum of the velocity data at the same streamwise positions considered for the analysis of the time

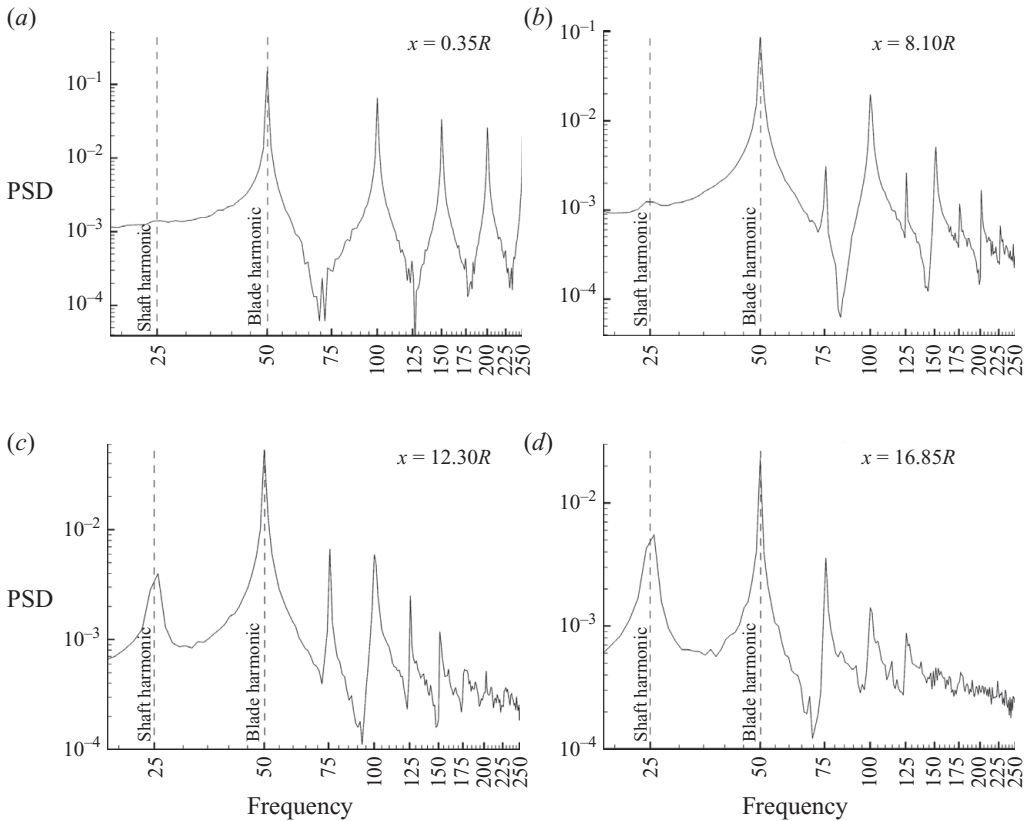


FIGURE 38. (a–d) Two-bladed propeller. Power spectrum of the radial velocity.

histories and the phase-averaged signals. An overview of the power spectra streamwise evolution is shown by the isocontours of figure 41.

In the power spectra of the near field, the fundamental frequency is correlated to the blade passage and thus corresponds to $f = nZ$ (i.e. $f = 50$ Hz for the two-bladed propeller, $f = 75$ Hz for the three-bladed propeller and $f = 100$ Hz for the four-bladed propeller; see figures 38–40).

In the transition and the far field, the streamwise evolution of the PSD of the velocity signals demonstrates a mechanism of energy relocation that involves the fundamental frequency and the first and second shaft harmonics. Indeed, the process of energy relocation does not occur through a single step with a direct energy transfer from the blade to the shaft harmonics (Felli *et al.* 2006), but involves other additional harmonics, fractions of the blade harmonic, in a multi-step mechanism. The characteristics of such a mechanism differ depending on the blade number, as shown in figures 38–41. More specifically these are as follows.

(i) *Two-bladed propeller.* At the beginning of the transition wake of the two-bladed propeller (i.e. $x \cong 8R$), two main contributions appear in the spectrum: the fundamental frequency at 50 Hz and a secondary contribution at the shaft harmonic, which increases more and more streamwise (figure 38a,b). At $x = 16.85R$ the process of energy transfer from the blade to the shaft harmonic is not yet over but it runs out further downstream at $J = 0.8$.

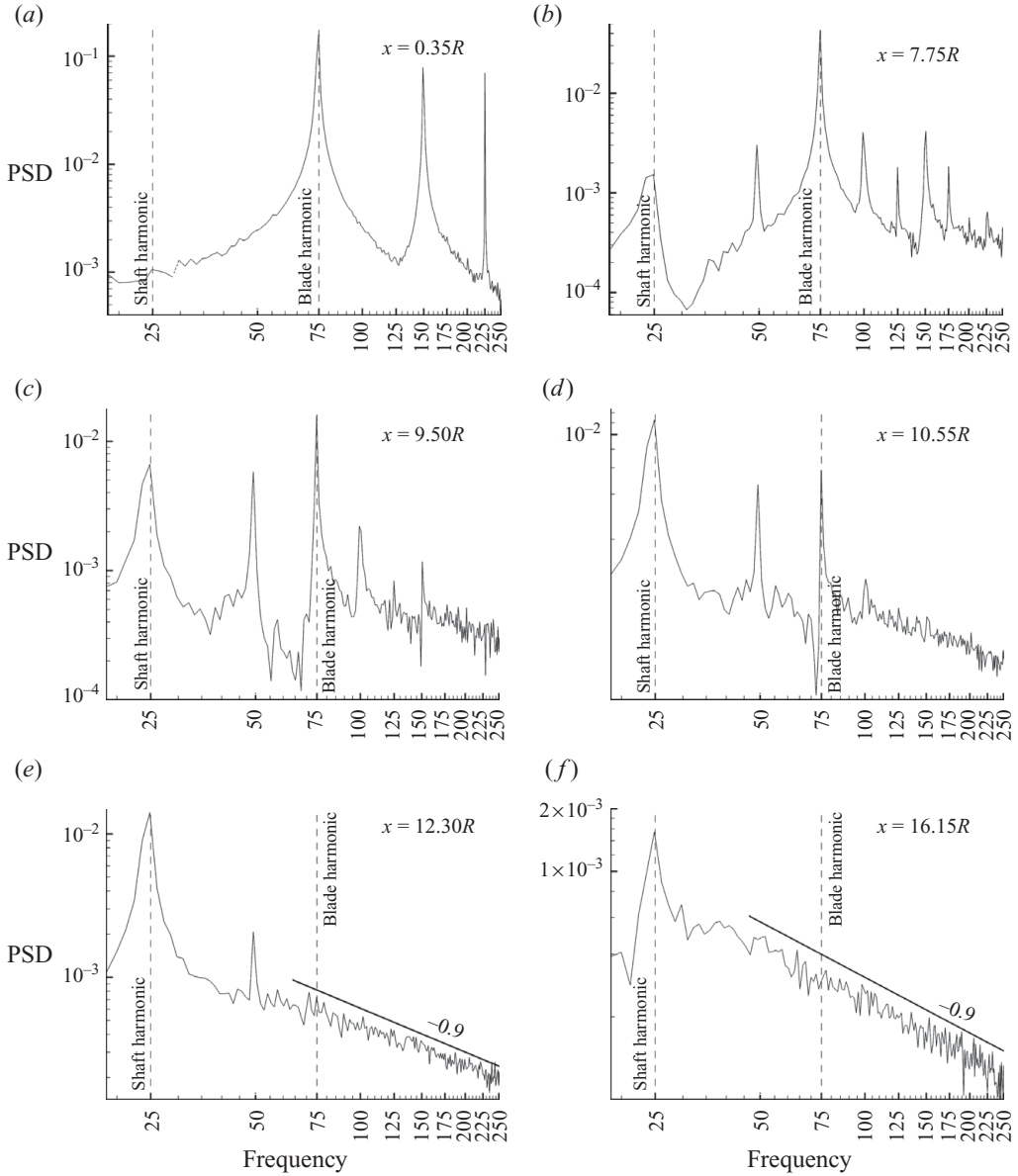


FIGURE 39. (a-f) Three-bladed propeller. Power spectrum of the radial velocity.

(ii) *Three-bladed propeller*. The wake transition is observed to occur around $x = 8R$, the spectrum showing the appearance of the first (i.e. 25 Hz) and second shaft harmonics (i.e. 50 Hz), in addition to the fundamental frequency (i.e. 75 Hz) (figure 39b). Therefore, in this case, the energy transfer involves the blade harmonic and the first and second shaft harmonics, in a two-step process. Firstly, the energy content at the blade harmonic moves to the first and second shaft harmonics, as confirmed by the increment of the peaks at 25 and 50 Hz and the simultaneous reduction of the contribution at 75 Hz. Thereafter, the energy at the blade harmonic and the second shaft harmonic flows into the shaft frequency, which is the only

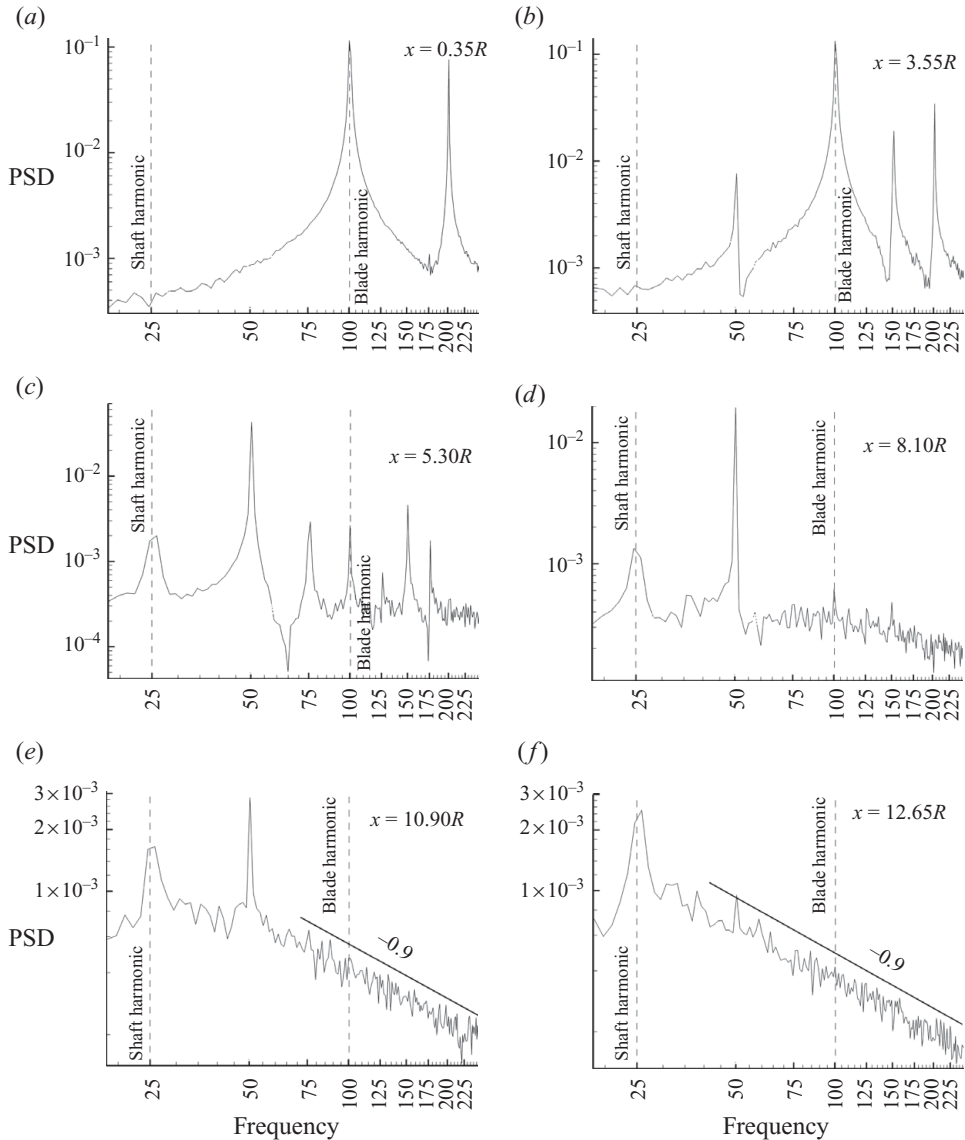


FIGURE 40. (a–f) Four-bladed propeller. Power spectrum of the radial velocity.

contribution of the spectrum from $x = 13R$. In this regime, power-law decay with exponent $k = -0.9$ occurs (figure 39f).

(iii) *Four-bladed propeller.* The process of energy transfer of the four-bladed propeller is characterized by a two-step cascade mechanism. In the first step, the energy transfer involves the harmonics at the blade- (i.e. 100 Hz) and half-the-blade harmonic (i.e. 50 Hz), without providing any significant contribution to the shaft harmonic (figure 40b). The peak at the shaft frequency appears further downstream, starting around $x = 5R$ (figure 40c). Nearly at $x = 7R$, the blade harmonic completely disappears from the spectrum and the process of energy transfer involves the contributions of the shaft frequency and half-the-blade frequency (50 Hz) (figure 40d). This second step of the cascade runs out around $x = 12R$ and the shaft harmonic

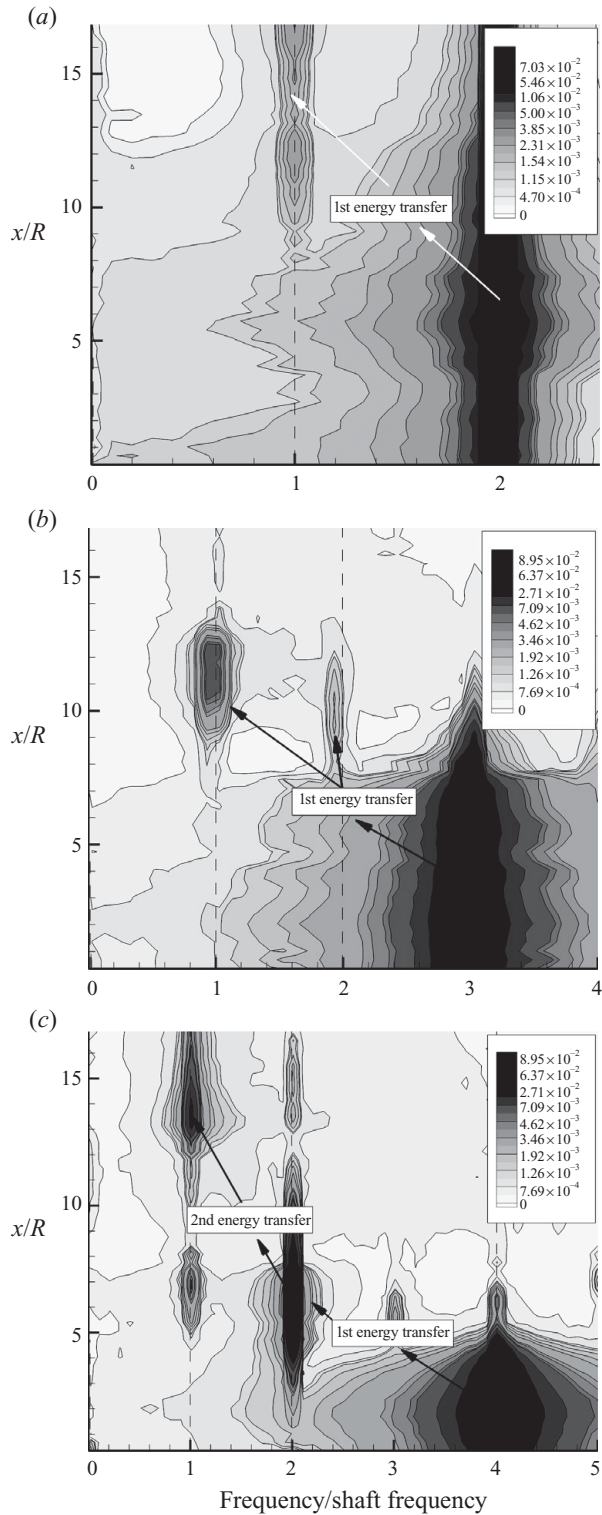


FIGURE 41. Evolution of the power spectrum of the velocity signals for the two- (a), three- (b) and four- (c) bladed propellers.

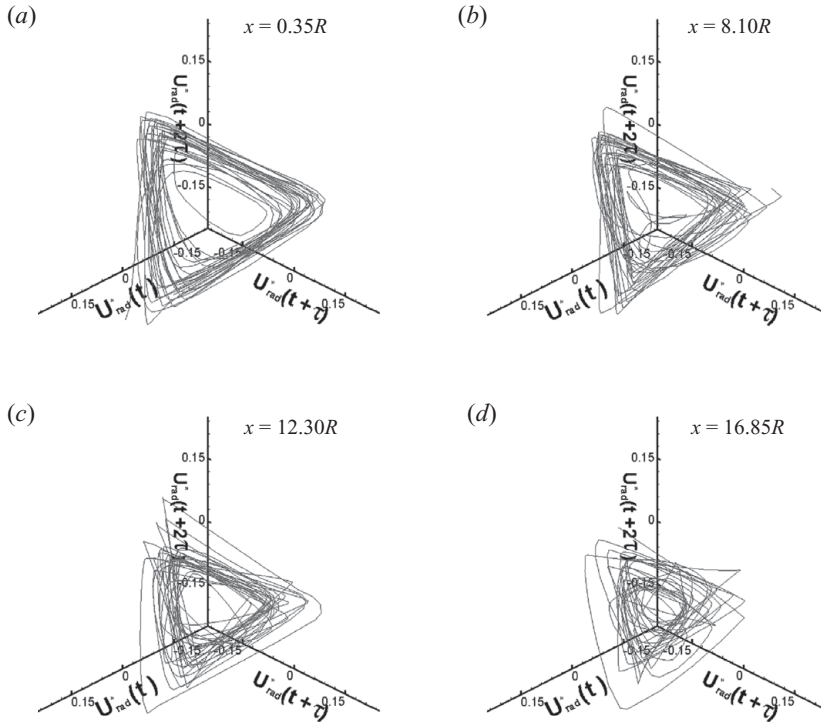


FIGURE 42. (a–d) Two-bladed propeller. Phase trajectories in the normalized pseudo-space $U_{rad}^*(t)$, $U_{rad}^*(t + \tau)$, $U_{rad}^*(t + 2\tau)$.

remains the only contribution in the PSD. The exponent of the power-law decay is $k = -0.9$, analogous to case of the three-bladed propeller (figure 40f).

Trajectories and phase states in the pseudo-phase space are represented in figures 42–44 in a 3D pseudo-phase space.

The representation in the pseudo-phase space shows a strange attractor with a complex shape, whose projection in the picture plane resembles that of a deformed triangle. This geometry, in which the phase trajectories describe zones of recurrent behaviour in the form of orderly periodicity, is clearly due to the on-average periodic nature of a signal with one fundamental frequency (Bergé *et al.* 1984). Therefore, the evolution of the phase states does not repeat the same circuitous phase space route periodically but describes different paths at each turn with a similar shape. This aspect is correlated to the turbulent nature of the signal that influences the dispersion rate of the space states at each period and, thus, the deviation among different turns in a trajectory.

The highly deformed shape of the attractor is the consequence of the complex nature of the signal that differs significantly from a sinusoid. Actually, the more the signal deviates from a sinusoid the more the trajectories diverge from a torus in the phase space (Bergé *et al.* 1984).

The shape of the attractor does not seem to show dependence on the blade number, as expected considering that (i) the shape of the velocity signal depends mainly on the geometrical characteristics of the blade, once the loading conditions are fixed; (ii) the amplitude and the slope of the velocity signal due to a single blade are nearly independent of the blade number, the propellers working at tip vortex identity;

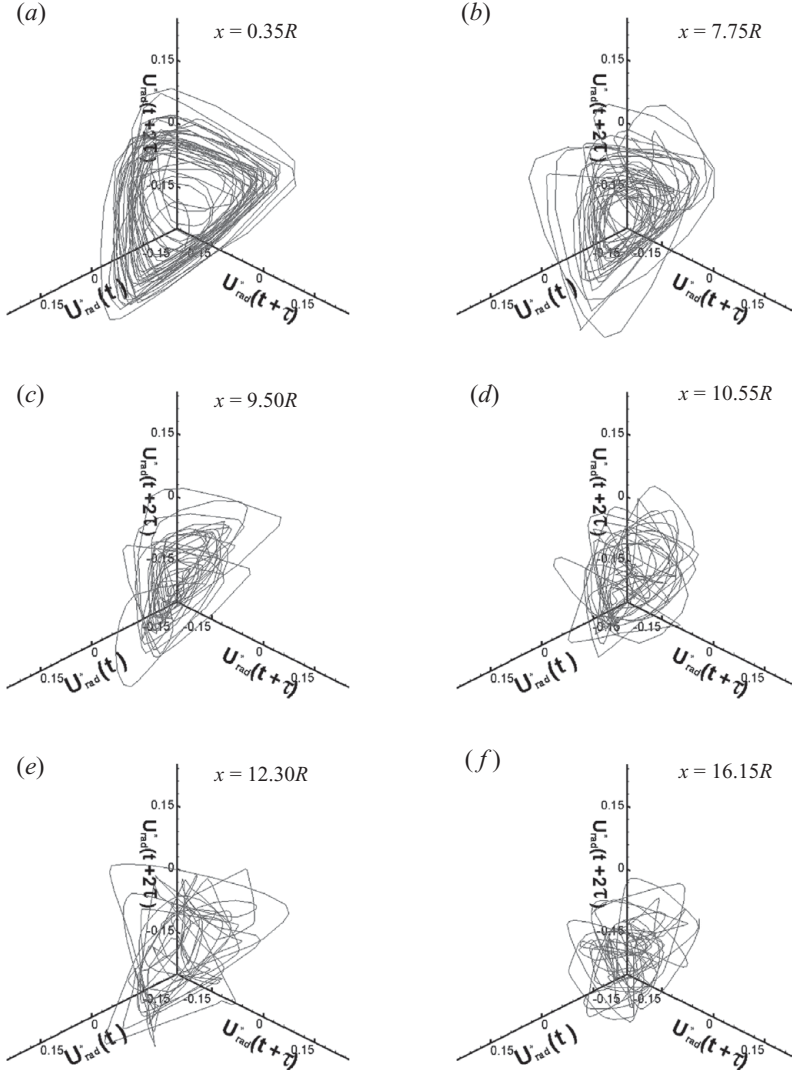


FIGURE 43. (a–f) Three-bladed propeller. Phase trajectories in the normalized pseudo-space $U_{rad}^*(t)$, $U_{rad}^*(t + \tau)$, $U_{rad}^*(t + 2\tau)$.

(iii) different values of the fundamental frequency do not influence the shape of the attractor.

Moving streamwise within the first periodic regime, the attractor preserves its shape even if it undergoes a gradual reduction of the taken volume and a more and more broaden boundary. This behaviour is physically the consequence of the streamwise increased levels of turbulence of the tip vortex (Jessup 1989; Stella *et al.* 2000; Di Felice *et al.* 2004) that causes smoothing of the velocity peaks as well as a dispersion of the phase states as mentioned earlier.

In this regard, it should be noted that the fluctuations of the velocity signals at a point of the grid depend on two aspects: (i) the high levels of turbulence in the tip vortex and (ii) the fluctuating positions of the tip vortex. In the near wake the former contribution is predominant, the tip vortex passage being regular and

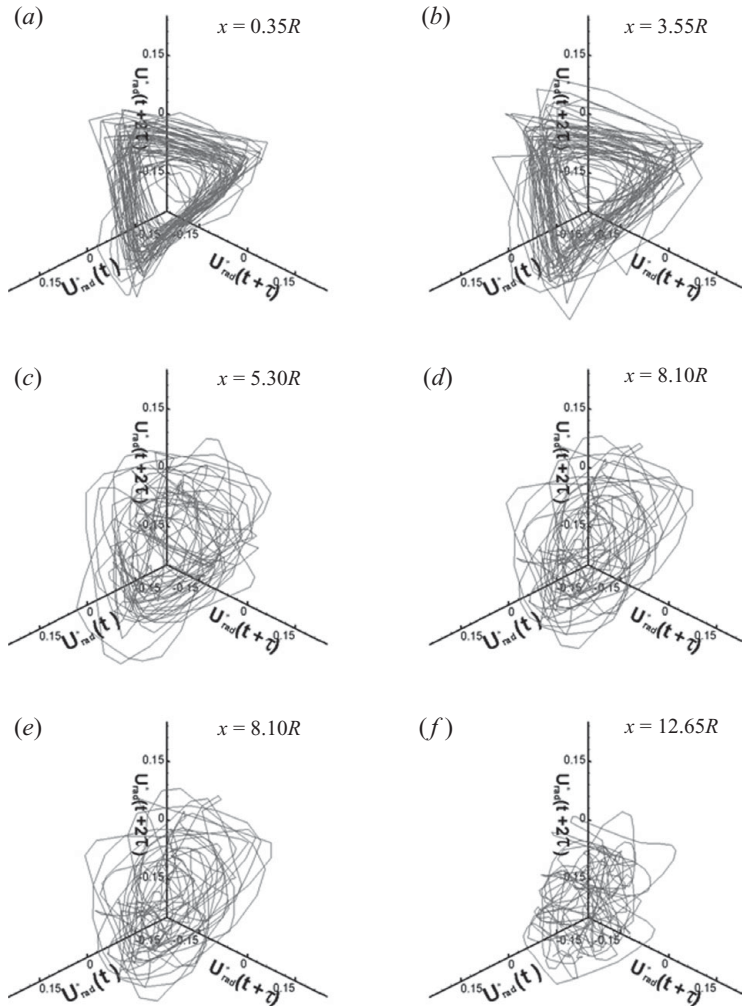


FIGURE 44. (a-f) Four-bladed propeller. Phase trajectories in the normalized pseudo-space $U_{rad}^*(t)$, $U_{rad}^*(t + \tau)$, $U_{rad}^*(t + 2\tau)$.

the oscillations small; the latter contribution becomes more and more predominant further downstream as a consequence of the strong distortions that the tip vortices undergo in the transition and the far wake (see §4.1.1.).

In the transition wake, phase trajectories lose the typical regularity of the near wake and describe more and more disordered paths in which the phase states tend to disperse in the shape of a cloud.

This trend is also confirmed by the behaviour of the maximal Lyapunov exponent (figure 45): the positive value of the Lyapunov exponent, due to the chaotic nature of the signal, increases streamwise, following approximately a zero-slope linear fitting in the near wake and a parabolic fitting thereafter.

In the zero-slope linear fitting region, the maximal Lyapunov exponent is $LE = 0.12 \pm 0.10$ on average that is nearly zero considering the turbulent nature of the tip vortices as well as their streamwise increasing fluctuations. The passage from the zero-slope linear fitting to the parabolic fitting region occurs nearly in

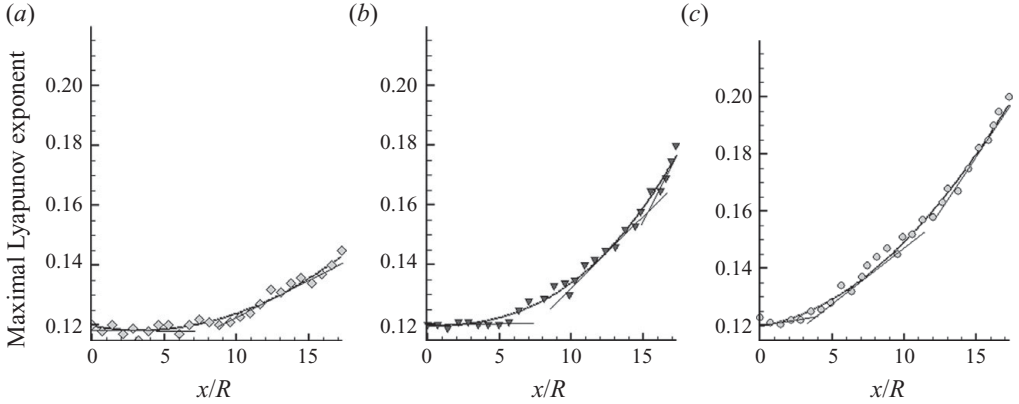


FIGURE 45. Evolution of the maximal Lyapunov coefficient for $Z=2$ (a), $Z=3$ (b) and $Z=4$ (c).

correspondence with the instability transition region (i.e. around $x=10R$ for the two-bladed propeller, $x=6R$ for the three-bladed propeller and $x=3.5R$ for the four-bladed propeller approximately). Here, assuming a more and more chaotic nature, the velocity time histories start to lose the nearly periodic nature typical of the near wake.

5. Conclusions and final remarks

In the present work the problem of the propeller wake evolution and instability was addressed experimentally. Specifically, the study dealt with the effect of the spiral-to-spiral distance and the number of blades on the mechanisms of destabilization and evolution of the tip and hub vortices in the transition and the far wake.

Time-resolved visualizations allowed us to highlight the dependence of the wake instability transition on the inter-spiral distance and, specifically, the streamwise displacement of the transition region at the increasing inter-spiral distance. Judging by the analysis of the visualizations, the destabilization of the tip vortices seems to come before that of hub vortices, independent of the blade number and the propeller loading conditions. This may suggest a possible cause-effect relationship between the two phenomena whose demonstration requires a specific study to be performed.

In the transition wake, the streamwise evolution of the tip vortices occurs through a multi-step grouping mechanism. Such a grouping mechanism is driven by the mutual inductance between adjacent spirals, according to the model of Widnall (1972) for a single helical vortex, and occurs differently on changing the blade number. More specifically, the analysis of the time-resolved visualizations and the power spectra of the velocity signal outlined the following behaviour for the propeller configurations with two, three and four blades.

(i) *Two-bladed propeller.* The energy transfer occurs through a direct passage from the blade to the shaft harmonics, that is the consequence of the pairing between the two tip vortices.

(ii) *Three-bladed propeller.* A two-step grouping process distinguishes the tip vortex evolution in a three-bladed propeller. In the first step, the spectrum is characterized by a direct energy transfer from the blade harmonic to the first and second shaft harmonics that is associated with an alternate grouping among adjacent filaments (a single filament with one filament pair). Specifically, the system of three tip vortices,

$T/3$ spaced originally, is reorganized to a system of one single and one filament pair, $T/2$ spaced, after the first grouping step. Thus, the blade harmonic is replaced by the first and second shaft harmonics: the former is associated with the passage of a specific vortex system (i.e. passage of one filament or passage of a filament pair) whose characteristic time is T , and the latter is associated with the passage of a perturbation (i.e. passage of a single filament, a filament pair, a single filament and so on), whose characteristic time is $T/2$. Further downstream, the second grouping results in a complete grouping of the three vortex filaments that transfer energy from the second to the first shaft harmonic, definitely.

(iii) *Four-bladed propeller*. The aforementioned cascade mechanism of energy transfer is the result of a double ‘period-halving’ process that accomplishes the grouping of two vortex filaments and two filament pairs in a filament pair and a group of four filaments, respectively.

In the far wake, the mechanism of evolution of the propeller vortical filaments is featured by a more and more chaotic evolution of tip vortices, highlighted by both the distortion of the phase states in the shape of a cloud and by the almost flat spectrum of the velocity signals.

In this region, a complex interaction between the hub vortex and the tip filaments of the three- and four-bladed propellers was observed to occur with a mechanism similar to that described in Ortega *et al.* (2003). The chaotic dynamics of the tip vortices in the far wake suggests that this interaction may have a random nature. Further downstream, the hub vortex undergoes a double-helix breakdown, whose fundamental frequency corresponds to the blade harmonic.

REFERENCES

- BENSOW, R. E., LIEFVENDAHL, M. & WIKSTROM, N. 2006 Propeller near wake analysis using LES with rotating mesh. In *26th Symposium on Naval Hydrodynamics*, Rome, Italy.
- BERGÉ, P., POMEAU, Y. & VIDAL, C. 1984 *Order within Chaos*. Wiley.
- CENEDESE, A., ACCARDO, L. & MILONE, R. 1985 Phase sampling in the analysis of a propeller wake. *Exp Fluids* **6**, 55–60.
- CHESNAKAS, C. & JESSUP, S. 1998 Experimental characterization of propeller tip flow. In *Proc. 22nd Symposium on Naval Hydrodynamics*, Washington.
- CONLISK, A. T. 1997 Modern helicopter aerodynamics. *Annu. Rev. Fluid. Mech.* **29**, 515–567.
- DI FELICE, F., DI FLORIO, D., FELLI, M. & ROMANO, G. P. 2004 Experimental investigation of the propeller wake at different loading conditions by particle image velocimetry. *J. Ship Res.* **48** (2), 168–190.
- FELLI, M. & DI FELICE, F. 2005 Propeller wake analysis in non-uniform inflow by LDV phase sampling techniques. *J. Mar. Sci. Technol.* **10**, 159–172.
- FELLI, M., DI FELICE, F., GUJ, G. & CAMUSSI, R. 2006 Analysis of the propeller wake evolution by pressure and velocity phase measurements. *Exp. Fluids* **1**, 1–11.
- FELLI, M., FALCHI, M., FORNARI, P. & PEREIRA, F. 2008a PIV measurements on an impinging swirl jet in a large cavitation tunnel. In *14th Intl Symposium on Applications of Laser Techniques to Fluid Mechanics*, Lisbon, Portugal.
- FELLI, M., GUJ, G. & CAMUSSI, R. 2008b Effect of the number of blades on propeller wake evolution. *Exp. Fluids* **44**, 409–418.
- FROUDE, R. E. 1989 On the part played in propulsion by differences in fluid pressure. *Trans. Inst. Naval Architects* **30**, 390–405.
- GASTER, M. & ROBERTS, J. B. 1977 The spectral analysis of randomly sampled records by a direct transform. *Proc. R. Soc. Lond. A* **354**, 27–58.
- GLAUERT, H. 1927. A general theory of the autogyro. Aeronautical Research Council, R&M N.1132.
- GOLDSTEIN, S. 1929 On the vortex theory of screw propellers. *Proc. R. Soc. Lond. A* **123**, 440–465.

- GRECO, L., SALVATORE, F. & DI FELICE, F. 2004 Validation of a quasi-potential flow model for the analysis of marine propellers wake. In *Proc. 25th Symposium on Naval Hydrodynamics*, St John's, Newfoundland, Canada.
- GUPTA, B. P. & LOEWY, R. G. 1974 Theoretical analysis of the aerodynamic stability of multiple, interdigitated helical vortices. *AIAA J.* **12**, 1381–1387.
- HILBORN, R. C. 2000 *Chaos and Nonlinear Dynamics*. Oxford University Press.
- HYUN, B. S. & PATEL, V. C. 1991 Measurements in the flow around a marine propeller at the stern of an axisymmetric body. *Exp. Fluids* **11**, 105–117.
- JESSUP, S. D. 1989 An experimental investigation of viscous aspects of propeller blade flow. PhD thesis, School of Engineering and Architecture, Catholic University of America.
- JOUKOWSKI, N. E. 1912 Vortex theory of a rowing screw. *Trudy Otdeleniya Fizicheskikh Nauk Obshchestva Lubitelei Estestvoznaniya*. **16**, 1 (in Russian).
- KERWIN, J. E. 1986 Marine propellers. *Annu. Rev. Fluid Mech.* **18**, 367–403.
- KLEIN, R., MAJDA, A. J. & DAMODARAN, K. 1995 Simplified equations for the interaction of nearly parallel vortex filaments. *J. Fluid Mech.* **288**, 201–248.
- KOBAYASHI, S. 1982 Propeller wake survey by laser Doppler velocimeter. In *Proc. Intl Symposium on the Application of Laser-Doppler Anemometry to Fluid Mechanics*, Lisbon.
- LANDGREBE, A. J. 1972 The wake geometry of a hovering rotor and its influence on rotor performance. *J. Am. Hel. Soc.* **17** (4), 3–15.
- LEISHMAN, J. G. 1998 Challenges in understanding the vortex dynamics of helicopter rotor wakes. *AIAA J.* **36** (7), 1130–1140.
- LEVY, H. & FORSDYKE, A. G. 1928 The steady motion and stability of a helical vortex. *Proc. Roc. Soc. Lond. A* **120**, 670–690.
- LIEFVENDAHL, M., FELLI, M. & TRÖNG, C. 2010 Investigation of wake dynamics of a submarine propeller. In *Proc. 28th Symposium on Naval Hydrodynamics*, Pasadena.
- LUGT, H. J. 1996 *Introduction to Vortex Theory*. Vortex Flow Press.
- MAGLER K. W. & SQUIRE H. B. 1953 The induced velocity field of a rotor. Aeronautical Research Council, R&M N.2642.
- MILLER, N., TANG, J. C. & PERLMUTTER, A. A. 1968. Theoretical and experimental investigation of the instantaneous induced velocity field in the wake of a lifting rotor. *USAAVLABS Tech. Rep.* 67–68.
- OKULOV, V. L. 2004. On the stability of multiple helical vortices. *J. Fluid Mech.* **521**, 319–342.
- OKULOV, V. L. & SØRENSEN, J. N. 2007 Stability of helical tip vortices in rotor far wake. *J. Fluid Mech.* **576**, 1–25.
- OKULOV, V. L. & SØRENSEN, J. N. 2010 Applications of 2D helical vortex dynamics. *Theor. Comput. Fluid Dyn.* **24**, 395–401.
- ORTEGA, J. M. 2001. Instability of helical vortices in a propeller wake. In *54th Annual Meeting of the Division of Fluid Dynamics*, American Physical Society, San Diego, CA.
- ORTEGA, J. M., BRISTOL, R. L. & SAVAŞ, Ö. 2003 Experimental study of the instability of unequal-strength counter-rotating vortex pair. *J. Fluid Mech.* **474**, 35–84.
- PEREIRA, F., SALVATORE, F. & DI FELICE, F. 2004a Measurement and modelling of propeller cavitation in uniform inflow. *J. Fluids Engng* **126**, 671–679.
- PEREIRA, F., SALVATORE, F., DI FELICE, F. & SOAVE M. 2004b Experimental investigation of a cavitating propeller in non-uniform inflow. In *Proc. 25th Symposium on Naval Hydrodynamics*, St John's, Newfoundland, Canada.
- PIZALI, R. A. & DUWALDT, F. A. 1962 Computation of rotary wing harmonic airloads and comparison with experimental results. In *Proc. 18th Annual Forum*, American Helicopter Society.
- PROPULSION COMMITTEE OF THE 23RD ITTC CONFERENCE 2002 Final Report and Recommendations to the 23rd ITTC. Venice, Italy.
- RANKINE W. J. 1865 On the mechanical principles of the action of propellers. *Trans. Inst. Naval Arch.* **6**, 13–30.
- RICCA, R. L. 1994 The effect of torsion on the motion of a helical vortex filament. *J. Fluid Mech.* **273**, 241–259.
- ROSENSTEIN, M. T., COLLINS, J. J. & DE LUCA, A. J. 1993 A practical method for calculating largest Lyapunov exponents from small data sets. *Physica D* **65**, 117–134.

- SAFFMAN, P. G. 1970 The velocity of viscous vortex rings. *Stud. Appl. Math.* **49**, 371–380.
- SALVATORE, F., PEREIRA, F., FELLI, M., CALCAGNI, D. & DI FELICE, F. 2006 Description of the INSEAN E779A propeller experimental dataset. *INSEAN Tech. Rep.* 2006-085.
- SALVATORE, F., TESTA, C. & GRECO, L. 2003 A viscous/inviscid coupled formulation for unsteady sheet cavitation modelling of marine propellers. In *Proc. CAV 2003 Symposium*, Osaka, Japan.
- SARPKAYA, T. 1971 On stationary and travelling vortex breakdowns. *J. Fluid Mech.* **45**, 545–559.
- STELLA A., GUJ, G., DI FELICE, F. & ELEFANTE, M. 2000. Experimental investigation of propeller wake evolution by means of LDV and flow visualizations. *J. Ship Res.* **44** (3), 155–169.
- TAKENS, F. 1981. Detecting strange attractors in turbulence. In *Lecture Notes in Mathematics*, vol. 898, pp. 366–381. Springer-Verlag.
- VERMEER, L. J., SORENSEN, J. N. & CRESPO, A. 2003 Wind turbine wake aerodynamics. *Prog. Aerosp. Sci.* **39**, 467–510.
- WIDNALL, S. E. 1972 The stability of helical vortex filament. *J. Fluid Mech.* **54**, 641–663.